A document submitted for the degree of

Doktor der Naturwissenschaften

A concept for personalised CT dosimetry using methods of machine learning

Marie-Luise Kuhlmann, geb. Steil

2025

AG Kröninger, Technische Universität Dortmund, Dortmund, 44227, Germany

This dissertation was submitted to the Department of Physics at the Technical University of Dortmund.

First examiner:	Prof. Dr. Kevin Kröninger
Second examiner:	Prof. Dr. Armin Lühr

Submission date:	07.11.2025
Defence date:	19.01.2026

Abstract

In the context of increasing number of computer tomography (CT) examinations, also the importance for fast and patient specific dose assessment grows. Machine learning (ML) offers a promising approach to achieve fast and user-friendly organ dose assessment in clinical CT workflows. Previous studies have shown that neural networks can reproduce Monte Carlo (MC)-calculated organ doses with reasonable accuracy; however, the representation of the radiation field properties, defining the spatial and energy distribution of the X-ray beam during acquisition, and the characterisation of the training data distributions vary widely. Furthermore, a comprehensive uncertainty assessment over the entire dosimetry process has not been addressed. This thesis presents a framework for personalised CT dosimetry based on ML methods, combining a validated newly implemented particle source for MC simulations, measurement-based radiation field characterisation and systematic uncertainty assessment at every stage of the process. In addition, the work investigated the influence of training data composition in regarding the role of synthetic and real patient geometry data. The proposed approach achieves accuracy comparable to previous studies, while providing a complete uncertainty assessment methodology.

Kurzfassung

Mit der steigenden Anzahl von Computertomographie (CT)-Untersuchungen nimmt auch die Bedeutung einer schnellen und patientenspezifischen Dosisabschätzung zu. Maschinelles Lernen (ML) bietet einen vielversprechenden Ansatz für eine schnelle und benutzerfreundliche Erfassung von Organdosen. Bisherige Studien haben gezeigt, dass neuronale Netze in der Lage sind, mit Monte Carlo (MC) berechnete Organdosen mit einer Genauigkeit von wenigen Prozent zu reproduzieren, wobei die Beschreibung der Strahlungsfeldeigenschaften, die die räumliche und energetische Verteilung der Röntgenstrahlung während der Aufnahme definieren, und die Charakterisierung der Trainingsdateneigenschaften stark variieren. In dieser Arbeit wird ein Ansatz zur personalisierten CT-Dosimetrie auf der Basis von ML-Methoden vorgestellt, der eine messtechnische Charakterisierung des Strahlungsfeldes, eine validierte, neu implementierte Partikelquelle für MC-Simulationen und eine systematische Unsicherheitsbestimmung in jeder Prozessphase umfasst. Darüber hinaus wurde der Einfluss der Zusammensetzung der Trainingsdaten hinsichtlich der Rolle synthetischer und realer Patientengeometriedaten untersucht. Der vorgeschlagene Ansatz erreicht eine mit früheren Studien vergleichbare Genauigkeit und bietet gleichzeitig eine umfassende Methodik zur Unsicherheitsbestimmung.

Statement of Contribution

This thesis is partly based on the content of one published paper, two conference papers and one publication in preparation. Each paper publication was co-authored by Dr. Stefan Pojtinger, the head of my working group 6.25 at PTB. The last publication in preparation additionally includes contribution of Dr. Jörg Martin from PTB working group 8.44.

The following list presents the publications and indicates the corresponding chapters in this thesis where content of these publications is presented.

1) M.-L. Kuhlmann, S. Pojtinger, “Implementation of a new EGSnrc particle source class for computed tomography: validation and uncertainty quantification”, PMB (2024) [1] (chapter 2.4, 3.1, 4.1)
2) M.-L. Kuhlmann, S. Pojtinger, “Generation of a representative synthetic phantom dataset for the training of neural networks in personalized CT dosimetry”, Proceedings Virtual Imaging Trials in Medicine 2024 (2024) [2] (chapter 2.5.2.1, 3.2.1)
3) M.-L. Kuhlmann, S. Pojtinger, “Impact of patient positioning on neural network organ dose estimation in CT”, Proceedings Virtual Imaging Trials in Medicine 2024 (2025) [3] (chapter 4.2)
4) M.-L. Kuhlmann, J. Martin, S. Pojtinger, “Use of synthetic data for training dose prediction neural networks in CT dosimetry” (preprint) [4] (chapter 2.5, 3.3.2, 4.2)

For all publications I was responsible for implementation, experimental setups, data collection, data analysis and the manuscript drafting for all chapters. Co-authors contributed discussion of conceptualization and results, and manuscript review. The development of the uncertainty estimation concept for the neural networks was assisted by Dr. Jörg Martin.

Parts of this dissertation were linguistically refined using AI-based language tools (PTB intern tools for translation and text optimization based on DeepL) to improve clarity and grammar. The conceptual content, data interpretation, and argumentation remain entirely my own.

Table of Content

List of Tables

List of Figures

1. Introduction

1.1 Background and Motivation

The invention of computer tomography (CT) in the early 1970s by Sir Godfrey Hounsfield started a new chapter of medicine, allowing new levels of diagnostic precision compared to two-dimensional imaging techniques. Dosimetry concepts followed the invention. In 1977, Jucius and Kambic introduced the pencil chamber and presented the first comprehensive CT dosimetry publication [5]. The Computer Tomography Dose Index (CTDI) was initiated in 1981 in the Unites States by Shope et. al. to "provide […] a means to characterize the doses resulting from CT procedures", characterizing the air kerma per slice in a cylindrical PMMA (polymethyl methacrylate) phantom [6].

CT underwent a major leap in development in the 1990s. Spiral CT [7] and multirow detectors increased imaging speed, patient comfort and the number of CT examinations. This trend is still present. Between 2007 and 2018, the number of CT scans in Germany increased by 25 % [8]. The introduction of preventive examinations such as lung cancer screening in Germany, started in 2024 (LuKrFrühErkV), can potentially increase the number of examinations even further.

The evolving CT technique needed to be followed by adaptations of dosimetry concepts. Spiral CT and increasing collimations required the mathematical concept of the CTDI to be rethought [9].

With the increasing awareness of possible risks from even low doses (linear no-threshold dose response theory) of ionizing radiation [10], many steps have been taken in recent decades concerning patient dose estimation. Over many decades several European research groups [[6], [7], [8]] investigated the calculation of effective dose using anthropomorphic phantoms. As one result conversion factors for effective dose estimation from CTDI measurements were calculated using radiation transport simulations [14]. Correction factors to consider patient size were introduced resulting in the size-specific dose estimate (SSDE) [15]. The effective dose is defined as the risk based weighted sum of specified organ doses and was meant to estimate risk concerning the stochastic effects of ionizing radiation.

The applications of effective dose values mentioned by the International Commission for Radiation Protection (ICRP) in ICRP report 147 are epidemiological studies concerning CT and choice of imaging techniques [16]. Both applications facing problems when based on effective dose calculated from CTDI values. Dose estimation in studies is often affected by lack of

personalization, which reduces the reliability [16]. Using the tabulated conversion factors to estimate effective dose from CTDI and DLP, does not account for tube current modulation, field inhomogeneities, differences in scan length and therefore for radiated body parts and organs, or individual body properties besides diameter. Hence, the patient dose estimation can only be seen as a broad estimation [17]. Using conversion factors also do not allow the calculation of individual organ doses.

In the context of imaging technique choice the comparison of effective doses via measured quantities, such as kerma area products (DAP) for cone beam CT or air kerma length products (DLP) in CT, is difficult [18]. Technical measures like CTDI, DLP, or DAP are not sufficient to characterize the radiation field of the respective device so precisely that conversion into effective dose can be done, suitable for modality comparisons [18].

Even though there were multiple works on rethinking CT dosimetry [[19], [20], [21], [22]] and adapting it to the current CT technology, the clinical practice of using technical measures like CTDI has not changed accordingly, as discussed by John Damilakis [23].

The problems arising from using CTDI-based effective dose estimation can be solved by using Monte Carlo (MC) radiation transport simulations, which offer high accuracy and flexibility. MC simulations are adaptable to the scanner-specific parameters and individual patient properties, allowing organ dose calculations[[24], [25], [26]]. However, despite their accuracy, the clinical use remains limited. Their implementation requires high computational resources, detailed patient segmentation and specialised expertise in radiation physics and modelling [23]. Additionally, the information necessary for this modelling are often not openly available. As a result, the use of MC simulation remains restricted to research applications.

To overcome some of these limitations, machine learning (ML) has emerged as a promising approach for CT dose estimation. Several studies have demonstrated the potential of ML-based approaches for fast scanner and patient-specific calculations (e.g. [27], [28], [29]).

1.2 Problem Statement and Objectives

In the context of clinical workflows, patient dose, especially organ dose assessment, needs to be user-friendly and fast. Being able to generate a database of reliable dose values, can serve as a valuable resource for researchers, enabling them to assess the effects of low doses while also optimizing clinical scanning protocols. Furthermore, a personalised dosimetry tool can be practical for comparing imaging modalities.

Machine learning can be one approach to achieving the goal of personalized CT dosimetry [30]. Several studies have demonstrated that ML models, particularly neural networks, can reproduce organ doses calculated by MC simulation with deviations up to 20 % (e.g. [28], [29]). Mayer et. al. [27] and Salimi et. al. [31] reproduced full three-dimensional (3D) dose distributions. A major difference among these studies lied in how they represent the radiation field properties in the network input. For instance, Mayer et. al. employed a water-equivalent patient geometry attenuation map, whereas Tzanis and Damilakis [32] used one-dimensional information such as mean Hounsfield unit values of organ tissues, tube current, patient position and water-equivalent diameter of the patient.

The selection and quality of the input quantities required by an ML algorithm for accurate dose prediction is a key research question. Equally important is the quality and statistical distribution of the training data. Many publications describe the patient cohort in terms of age and sex, while Maier et al. [27] additionally report the range of effective patient diameters covered by the data. Other potentially relevant parameters such as patient height, organ volumes or adipose tissue content are rarely discussed. The distribution and control of these features is often limited by data availability and heterogeneity. The use of synthetic patient geometries as training data offers significant potential in this context, as it allows for controlled data distributions and systematic exploration of influencing factors. While synthetic anatomical models and data augmentation have demonstrated considerable potential in the field of diagnostic applications of machine learning[[33], [34]], their utilization in personalised CT dosimetry remained open. This thesis investigates the potential of synthetic data in machine learning-based personalised dosimetry and to evaluate the efficacy of integrating real and synthetic datasets.

Although both MC-based simulation frameworks for CT dosimetry and ML-based approaches for personalised dose estimation are presented in the literature, comprehensive uncertainty assessments are typically missing from the methodological validation. A complete and transparent uncertainty assessment covering all stages - from data generation to model prediction - remains an open challenge.

The overall aim of this thesis was to establish a framework for personalised CT dosimetry using ML methods. The work explicitly addressed the uncertainty evaluation at every stage of the process, implementing a new particle source based on measurement data and additionally utilizing measurement-based radiation filed characteristics as model input. This input is realized as an 3D-air kerma attenuation curve in water, based on measured energetic and spatial photon distribution.

The specific objectives of this work were the following:

1) Implementation of a new particle source for the calculation of CT dose distributions, which can be adapted to any CT scanner using a simple set of measurements, including metrological validation and uncertainty evaluation.
2) Development of ML based patient dose estimation approach. This includes the generation of a representative training dataset from validated MC simulations, investigating the potential of the use of synthetic patient geometry data, and the design and training of a neural network model capable of estimating patient- and organ-specific dose values from measurement-based radiation field inputs.
3) Integration of uncertainty analysis into ML-based dosimetry, by propagating training data uncertainty and analysing training stability

2. Materials and Methods

This chapter presents the theoretical foundations, simulation techniques, experimental procedures and computational methods used in this work.

It begins with a description of computer tomography principles (2.1) and CT dosimetry (2.2) introducing key dosimetric quantities and measurements. Section 2.3 provides an overview of Monte Carlo simulations for radiation transport, covering fundamental principles, types of cross-sections, sampling methods, modelling of photon and electron interactions, along with relevant transport parameters.

Building on this foundation, section 2.4 presents the development and integration of a new particle source model for CT dose calculations. This includes measurement procedures, the implementation within the simulation environment, experimental validation steps and associated uncertainty quantification.

Section 2.5 introduces machine learning concepts, focusing on neural networks, which are employed in the subsequent deep learning-based dose prediction framework. It additionally outlines the generation of training datasets required for neural network development, including simulations with virtual patient data (XCAT phantoms), real patient data and preprocessing steps. It finally presents the design, implementation and validation of the dose calculation U-Net, including training procedures and an analysis of the associated uncertainties.

2.1 Computer Tomography

Computer tomography is a medical imaging modality that reconstructs sliced 3D-images of patients using the difference in X-ray attenuation characteristics of various tissue types. A schematic of a CT system is shown in **Figure 1**. The X-ray tube A) rotates around the patient together with bowtie filter B) and the collimators C), generating a series of projection signals recorded by the detector array D). The object to be imaged is placed on the patient table E).

The photon field used for imaging is defined by the components A) – C). The X-ray tube, typically operated with a tube voltage U between 70 kV and 150 kV, produces the primary photon spectrum with an intensity defined by the tube current I.

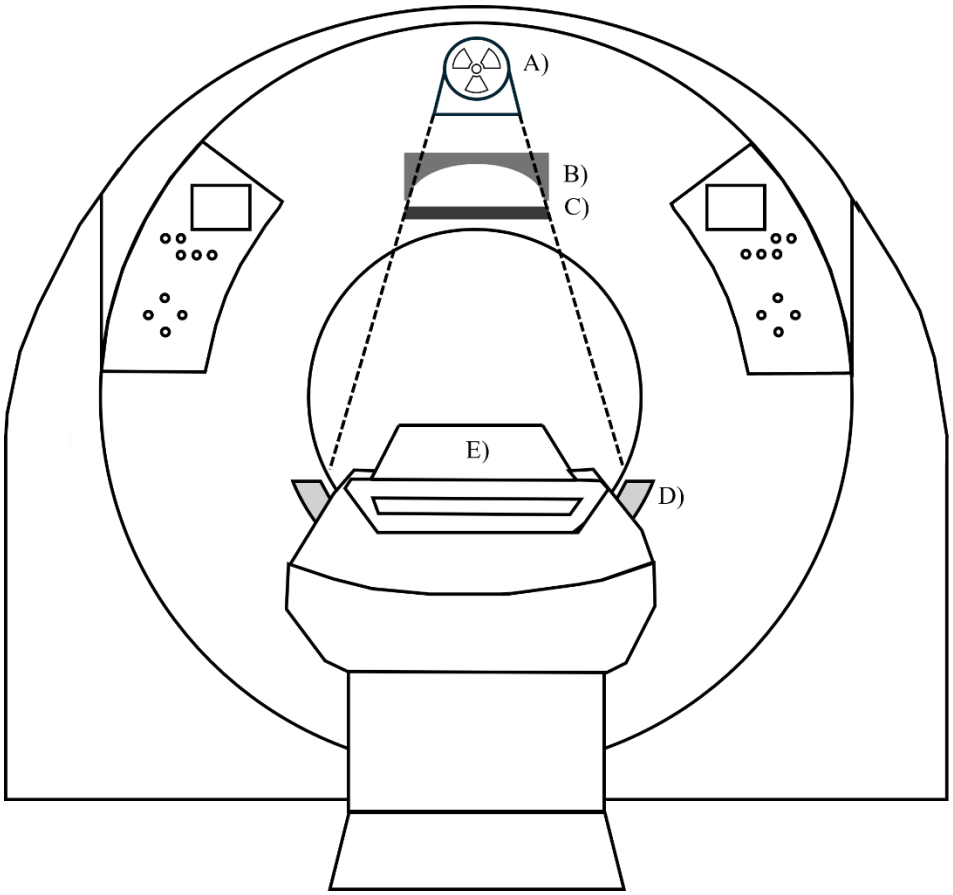

Figure 1. Schematic drawing of a Computer Tomography System and the basic components: A) X-ray tube, B) Bowtie-Filter, C) Collimator, D) Detector and E) Patient Table.

In clinical practice the CT output intensity is characterized by the time current product $Q = I \cdot t$, which is the product of tube current I and tube rotation time t. The bowtie or shaping filter modulates the photon fluence along in transversal patient axis. Due to the non-uniform patient thickness in this direction, the filter compensates for the attenuation differences, thereby yielding a more uniform detector signal. The collimators restrict the beam in longitudinal patient direction and determine the amount of detector rows radiated at the same time.

The measured projection data, commonly referred to as sinograms, are subsequently processed through mathematical reconstruction techniques into a volumetric image.

The CT scanner used in this work was an Optima CT 660 (GENERAL ELECTRICS, Chicago, IL, USA, S/N: 108502CT01). It is equipped with a patient table made from carbon-fiber-reinforced plastic and an X-ray tube with a tungsten anode, which can operate at four different tube voltages of 80 kV, 100 kV, 120 kV and 140 kV. The X-ray tube had an anode angle of 7 °. Collimation could be set to different values. In this work a collimation of 40 mm was used.

2.2 CT Dosimetry

In CT dosimetry, air kerma is the most used measured quantity. When referring to patient risk the effective dose and organ doses are calculated. In this chapter, the dosimetric quantities used in this work are explained and the measurement procedures are described. The following definitions of the dosimetric quantities are based on ICRU Report 60 [35], ICRU Report 90 [36] and for the clinical relevant definitions ICRU Report 87 [37].

2.2.1 Dosimetric Quantities

To describe a photon radiation field, the simplest quantity is the particle fluence

$$\Phi = \frac{dN}{dA} = \frac{\sum \Delta s}{dV}. \tag{1}$$

It is defined as the number of particles N that cross an area A and therefore has the unit cm^{-2}. As shown in equation (1) it can also be described as the sum over the particle track length Δs in an elementary sphere with volume dV.

The derivative of the particle fluence by the energy is named spectral fluence $\Phi_E = \frac{d\Phi}{dE}$.

In dosimetry the goal is to evaluate the energy transfer of the photon radiation to a certain material. The energy transfer can be described as a two-stage process. The term kerma stands for "kinetic energy released per unit mass" and is the quantity describing the first part of the energy transfer process. It describes the amount of initial kinetic energy transferred to secondary charged particles E_{tr}, liberated by uncharged ionizing particles in a mass element dm. The kerma K can therefore be formulated as

$$K = \frac{dE_{tr}}{dm}. \tag{2}$$

The transferred energy

$$dE_{tr} = \mu_{tr} \cdot dl \cdot E \cdot N \tag{3}$$

depends on the number of incident photons N, the photon energy E and the interaction probability characterized by the energy transfer coefficient μ_{tr} and the thickness of the mass element dl. With this expression and $dm = \rho \cdot dV$, as the product of the material density ρ and the volume element dV, equation (2) can be expressed as

$$K = \frac{\mu_{tr}}{\rho} \cdot E \cdot \left[\frac{N \cdot dl}{dV}\right] = \frac{\mu_{tr}}{\rho} \cdot E \cdot \Phi. \quad (4)$$

The term in the square brackets is the sum of all track length in the volume element, which is the particle fluence as described in equation (1). For a spectral photon beam in air equation (5) converts to

$$K_{\text{air}} = \int_0^{E_{max}} E \cdot \Phi_E \cdot \left(\frac{\mu_{tr}(E)}{\rho}\right)_{\text{air}} dE \ . \quad (5)$$

In the second stage of the energy transfer, the charged particles transfer their energy. The absorbed dose D is defined

$$D = \frac{d\bar{\varepsilon}}{dm} \quad (6)$$

as the mean energy $d\bar{\varepsilon}$ imparted in a mass element dm. The unit of absorbed dose and air kerma is Gy, with $1\ Gy = \ 1\ J \cdot kg^{-1}$.

The described quantities air kerma and absorbed dose can be measured using calibrated ionisation chambers. An additional measurement quantity is the air kerma length product KLP, measured with a pencil chamber, which integrates the kerma along its active length. The unit is of KLP is $cm \cdot Gy$.

In the clinical environment more complex quantities like the CTDI and dose length product (DLP) - not to confuse with KLP - are used to quantify the radiation field of CT scanners. However, the determination of CTDI and DLP is based on simple air kerma length product measurements. The CTDI first introduced in 1981 is still a dominant dose measurement concept in clinical practice and is theoretically defined as

$$CTDI_{\infty} = \frac{1}{nT} \int_{-\infty}^{\infty} K(z)\mathrm{d}z \quad (7)$$

with $K(z)$ describing the air kerma in a phantom in dependence of the position z along the scan axis. The nT term is the product of the number n of tomographic section imaged in a single axial scan (one rotation of the X-ray tube) and the nominal width of this section along the z axis. It can also be described as the axial scan interval. The $CTDI_{\infty}$ was described as the measure of the average absorbed dose at the centre of a scanned volume, produced by multiple gantry rotations, assuming the scan length is sufficient to reach its asymptotic upper limit. Hence the

integration over an infinite length is not possible, the $CTDI_{100}$ was introduced using an integration length of $100\ mm$, the length of a typical pencil chamber.

The average $CTDI_{100}$ across the field of view of an CT scanner can be calculated by

$$CTDI = \frac{2}{3}\ CTDI_{100,\text{peripheral}} + \frac{1}{3}\ CTDI_{100,\text{central}}. \tag{8}$$

The value can be measured as the weighted sum of the mean value $CTDI_{100,\text{peripheral}}$ of the four peripheral values and one central value $CTDI_{100,\text{central}}$ of an CTDI phantom as depicted in **Figure 8**. The measurement is performed for one 360° rotation of the X-ray tube. The dose length product

$$DLP = CDTI \cdot l \tag{9}$$

is than defined as the product of CTDI and the scan length l.

Personalized dosimetry uses quantities that cannot be measured directly, e.g. the organ doses. The organ dose D_{organ} is defined as the absorbed dose in the tissue of the organ. Another commonly used measure is the effective dose E_{eff}. This quantity is defined in such a way that it should correlate with the risk of developing cancer because of the irradiation. The effective dose

$$E_{\text{eff,organ}} = \sum_{T} D_T \cdot w_T \tag{10}$$

is a weighted sum of specified tissue doses D_T, weighted with risk related factors w_i, which were determined from epidemiology, radiobiology and population-based risk modelling [14, p. 103]. By using tabulated values for conversion factors w from the European guideline for quality assurance [13], an estimate for the effective dose can be calculated by

$$E_{\text{eff,calc}} = DLP \cdot w\ . \tag{11}$$

To account for the patient size, correction factors f_{size} were defined by the American Association of Physicists in Medicine in the AAPM report 204 [15].

The size specific dose estimate $SSDE = CTDI \cdot f_{\text{size}}$, can be used for effective dose estimates in the same way as the CTDI, but is not recommended in clinical use:

$$E_{\text{eff,SSDE}} = SSDE \cdot l \cdot w\,. \tag{12}$$

2.2.2 Dosimetric Measurements

Air kerma can be measured with ionisation chambers. An ionisation chamber is a gas filled cavity with two electrodes. Between the electrodes an electrical voltage is applied. The air is ionised by the radiation and the produced charge moves along the electric field, which results in a measurable charge M_Q. To convert the charge into air kerma

$$K_{air} = M_Q \cdot N_{K_{\text{air}},Q} \cdot k_\rho, \tag{13}$$

a calibration coefficient $N_{K_{\text{air}},Q}$ and an air density correction k_ρ must be applied.

All measurements in this work were conducted using an RC0.6 Farmer-type ionisation chamber (RADCAL, Monrovia, CA, USA, S/N: 9414) as shown in **Figure 3**. The charge collected in the chamber was measured with a UNIDOS electrometer (PTW, Freiburg, DE, S/N: 100006). Time-resolved data acquisition was achieved by combining the RC0.6 chamber with the ACCU-Gold read-out system (RADCAL, Monrovia, CA, USA).

The chamber was calibrated against the primary standards of Physikalisch-Technische Bundesanstalt (PTB) for radiation qualities Q RQT8, RQT9 and RQT10, as defined in IEC 61267:2005. The air density correction factor

$$k_\rho = \frac{p_0}{p} \cdot \frac{T}{T_0}, \tag{14}$$

corrects all measured values for the air density at $T_0 = 20$ °C and $p_0 = 1013.25\ hPa$ using the temperature T and atmospheric pressure p measured during the experiment. Air pressure during the measurements was continuously monitored using a pressure sensor, model 278 (SETRA, Boxborough, MA, USA, S/N: 3997310). The air temperature was recorded with a PT100 (resistance thermometer), which had been calibrated at the PTB.

2.3 Monte Carlo Simulation of Radiation Transport

The Monte Carlo method can be used to solve complex mathematical problems. For radiation transport, the Boltzmann transport equation describes the interaction between radiation and matter. In this case, the Monte Carlo method is a statistical method based on random numbers to simulate an ensemble of particles based on known cross-sections (see 2.3.1). The statistical estimator for a physical quantity can be determined by summing the contributions of the individual particles. Statistical uncertainty can be reduced by using many particles to exploit the law of large numbers, which states that the average of a result obtained from a large number of independent samples approximates to the true value [38].

The fundamental principle of radiation transport calculations is the stepwise tracking of each particle along its trajectory until it either leaves the simulation geometry, or its energy falls below a defined energy threshold due to interactions. The step length, the interaction type at the end of each step and the resulting particle properties are sampled from probability distributions as described by Kawrakov et. al. [39].

2.3.1 Cross-section Types

The named probability distributions are based on measured material and energy-dependent interaction characteristics, the cross-sections. There are three types of cross-sections as described in [40].

The microscopic cross-section σ can be seen as an "effective area" of an atom for a given particle type, particle energy E and interaction type. The total cross-section $\sigma(E) = \sum \sigma_i(E)$ is the sum of the cross-section for each interaction.

The macroscopic cross-section describes the probability of an interaction per unit length. For photons, this cross-section is called attenuation coefficient μ and is defined for a given density ρ, with $\mu(E) = \rho \cdot \sigma(E)$. It describes the loss in photon number with increasing depth in the material.
For electron interaction, the describing quantity for interaction probability is stopping power $S(E)$. In contrast to photons, it characterizes energy loss and not the decrease in particle number.

To describe the final state variables of a scattered particle, differential cross sections are used, as they specify any energy or directional dependencies:

$$\frac{d\sigma_i(E,E')}{dE'}, \frac{d\sigma_i(E,E',\Omega)}{dE'd\Omega},$$

with E and E' describing the energy before and after interaction and the angle Ω characterizing the change in direction.

2.3.2 Sampling Methods

Monte Carlo simulations of radiation transport are based on probability distributions describing the different properties of the particles to be transported. The sampling from probability distributions can be utilized through several different methods; however, only those used in this work are discussed here.

The inverse sampling method [41] requires a defined probability density function (PDF) $p(x)$ of the variable x. The cumulative distribution function (CDF) $F(x) = \int_0^x p(x)\,dx$ is defined as the integral of the PDF. Using the inversion method the sampling of x can be done by generating a uniform random number $r \in [0, 1]$ and evaluating the inverse of the CDF for r:

$$x = F(r)^{-1}. \tag{15}$$

In some cases, the inversion of a function is difficult to determine. The so-called alias method [42] is an efficient method for sampling from discrete distributions. The distribution is converted into a form that allows sampling to be carried out in constant time $O(1)$ by precomputing two tables, a probability table and an alias table. The method is realized by a so-called "decision rule", which enables a reduced representation of the potential results. This rule is applied in a threshold probability and a replacement choice (alias table), which is referred to as an "alias". As part of the sampling process, a random index is first determined, ensuring that the probability of each result is the same. A second random number is then used to decide whether to keep the selected result or switch to its alias. The process is characterized by using only two uniform random numbers.

2.3.3 Photon Transport

Photons interact with matter through various energy dependent mechanisms, the most significant being absorption (photoelectric effect), incoherent scattering (Compton scattering) and pair production. In the case of coherent scattering, Rayleigh and Thomson scattering are the most important ones to mention. With extremely high photon energy, photonuclear reactions can also occur. The energy range for photons in x-ray diagnostics is approximately 10 keV – 150 keV. Therefore, pair production (minimal photon energy of 1.022 MeV required) and photonuclear reactions are impossible in this energy range. In **Figure 2** the interaction cross sections for water are shown. As the figure shows, the photoelectric effect and Compton

scattering dominate the energy range of X-ray diagnostics (red area) in water. The interaction probabilities for human tissue are very similar, which mainly consists of water.

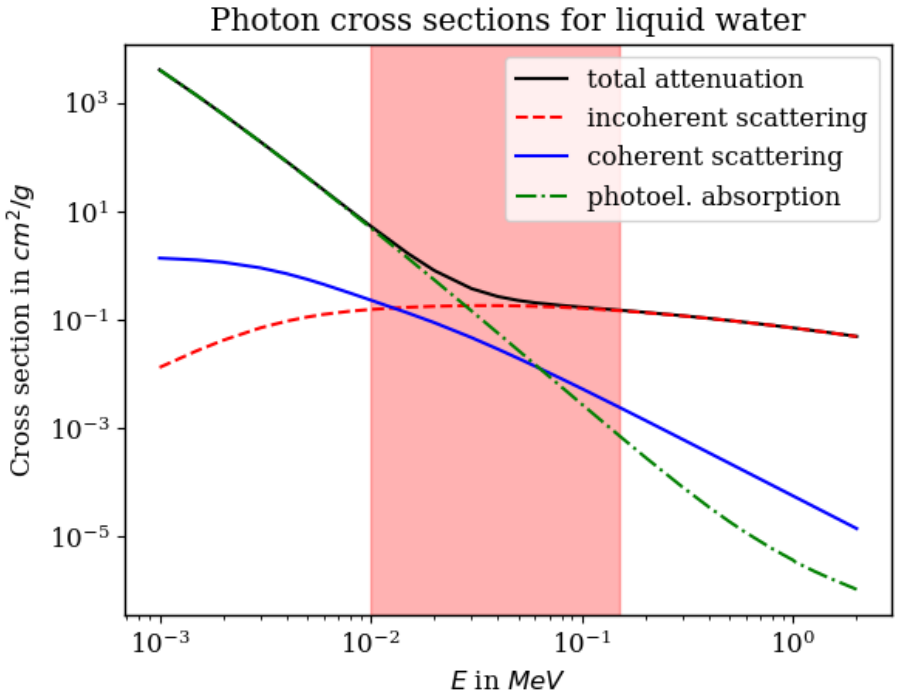

Figure 2. Energy dependent photon cross sections for liquid water [43], showing the total attenuation and the different interaction components. The red area shows the energy range of diagnostic X-rays.

Based on this interaction properties, four steps are necessary to simulate the transport of a photon with given energy E and direction $\vec{d}$ through matter as described in [40]. The distance to the next interaction x can be sampled from the particle's energy using the mass attenuation coefficient μ for a constant medium m. The interaction PDF is defined as

$$p(x) = \mu(E, m) \cdot e^{-\mu(E,m) \cdot x}. \tag{16}$$

The inversion method as described in 2.3.2 allowed the interaction distance to be sampled using a random uniform number r and evaluate the following equation:

$$x = -\frac{\ln(r)}{\mu}. \tag{17}$$

The particle transport is done in a straight line in the incident particle direction $\vec{d}$ for the distance x. At the interaction point, the interaction is sampled using the microscopic cross sections describing the probability for each interaction type as shown in **Figure 2**.

The interaction probability for each interaction is calculated as the ratio

$$\omega_i = \frac{\sigma_i}{\sigma} \tag{18}$$

of the interaction cross-section for the individual mechanism σ_i and the total interaction cross-section σ.

In the final step the final state of the photon using the differential cross-section is determined. For example, in the case of the Compton effect, both the scattering angle and the resulting energy change are sampled.

2.3.4 Electron Transport

Electron transport as described in [40], considerably more complex, primarily due to the electron charge, which significantly increases cross-sections compared to uncharged particles like photons and resulting in multi-scattering events. In the process of slowing down electrons interact thousands of times and their energy loss can be described as nearly continuous. Due to these interactions, they follow a curvilinear path.

Electrons interact with matter by four processes. When an electron interacts with another electron in the atomic shell via its charge over a relatively large distance, the bound electron can be knocked off, called ionisation, or the interaction changes the energy level of the electron, called excitation. This kind of interaction is called soft collision, due to the small amount of transferred energy. Soft collisions are the most common type of interaction. Hard collisions are interactions between the two electrons over a short distance and with large energy transfers. The interaction releases a “knock-on” electron, which has large kinetic energy and can induce ionisation itself. The atomic nucleus also contains charged particles and can interact with electrons. If the interaction results in a direction change with no energy transfer, it is called elastic scattering. If an energy loss occurs, the transferred energy is emitted as a so-called bremsstrahlung photon, therefore it is a bremsstrahlung interaction. The interaction with the atomic nuclei is the main reason for the convoluted electron path through matter.

Different methods are used to overcome the challenges of continuous energy loss and curvilinear particle trajectories for electron transport in Monte Carlo codes. Simulating every step and interaction of an electron would be too time-consuming. The condensed history method (CH) [44] groups a series of scattering steps and accounts for the scattering angle by using

multi-scattering theory. The energy loss is modelled either continuously or by large energy transfers and the production of a secondary electron.

2.3.5 Monte Carlo Transport Parameter

When using Monte Carlo methods for radiation transport, several parameters determine the transport and interaction behaviour. For the MC Code EGSnrc, used in this work, they are described in NRCC Report PIRS-701 [45]. Most important are the thresholds for the transport of primary particles and the production of secondary particles. For EGSnrc the transport cutoffs are called ECUT for electrons and PCUT for photons. The particles are transported until they leave the geometry or if their energy falls under the defined cutoff-energy. If the energy of a particle is lower than the defined threshold, the energy of the particle is deposited locally, except for positrons. For positrons, the annihilation photons can escape.

The thresholds to produce secondary particles are called AE and AP. AE defines the minimal energy of a secondary electron so that the interaction is handled discretely and the secondary electron is followed through the simulation geometry. For an energy lower than AE, the energy is treated as part of the continuous energy loss along the primary particle track. AP describes the threshold for bremsstrahlung photon production.

Another important parameter is the cross-section database. As described above, the cross-section data determines the interaction probabilities in the simulation. In EGSnrc, there are different options to choose from, and different effects can be turned on and off. In this work, the mcdf-xcom database [43] was used for the photon cross-section parameter. It contains data for the photoelectric effect, Raleigh scattering and pair/triplet production. The mcdf-xcom database provides theoretically determined cross section data. It is based on the Multiconfiguration Dirac-Fock (mcdf) mechanism as described in ICRU Report 90 [36], which accounts for relativistic effects and electron correlation.

2.4 Implementation of a New Particle Source

For the training data generation for the neural network, it was necessary to be able to calculate 3D-dose distributions. In a previous publication from our group [46], an experimental method for characterizing the spectral photon fluence of any CT scanner was presented. This method involves a simple set of measurements that can be performed under clinical conditions. It determines the spectrum of the CT scanner by measuring the aluminium attenuation curve and assesses the shape of the bowtie filter by angle-dependent air kerma measurements.

Importantly, this approach does not require access to proprietary manufacturer information. Building on this technique, our group developed a comprehensive personalised dosimetry approach for CT, which is described in detail in [47]. This approach used ImpactMC, a discontinued commercial software [48]. To advance this line of research the EGSnrc MC toolkit [39], particularly its C++ extension modules, was used to implement a customizable CT scanner source. EGSnrc is widely used for high-accuracy radiation transport simulations and offers multiple user codes for different objectives. For instance, the new implementation of the particle source allows the simulation of dosimetric quantities using an ionisation chamber model and image data (egs_cbct) using the same MC algorithm and simulation settings.

The implementation and validation of the source is part of this thesis and was published in [1] by the PhD candidate.

2.4.1 Measurement Procedure of CT Source Model

To characterize the radiation field of a CT scanner, there are two important pieces of information to determine: the energy distribution and the spatial distribution of the radiation. To characterize the energy distribution, the spectral photon fluence Φ_E in the centre of the gantry is needed.

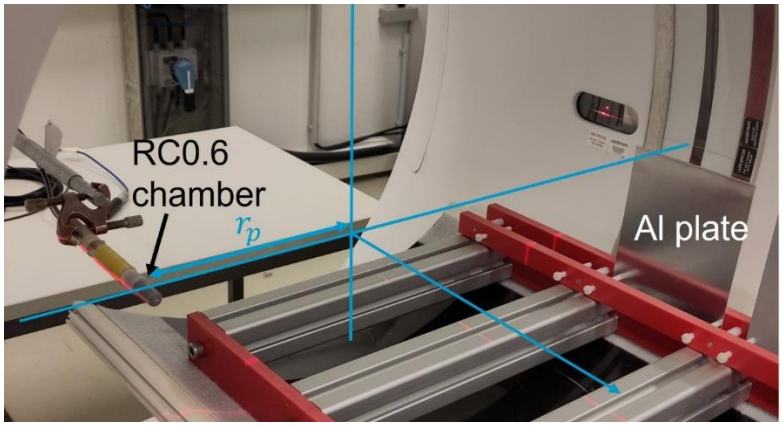

Figure 3. Experimental setup for measuring the aluminium attenuation curve and form filter characteristics. An RC0.6 chamber was placed approximately 25 cm from the gantry centre and aluminium sheets of varying thickness were aligned with the chamber. The bowtie filter profile was recorded in air with the patient table removed, from [1], Licensed under CC BY 4.0 (https://creativecommons.org/licenses/by/4.0/).

The spectral photon fluence were derived by analysing its aluminium attenuation properties. A Radcal RC0.6 ionisation chamber was placed at $r_p = 25\ cm$ from the isocentre within the gantry. Aluminium plates of increasing thickness were mounted on a holder positioned on the patient table (see **Figure 3**). The chamber, connected to an ACCU-Gold digitizer, recorded time-

resolved signals as the X-ray tube rotated and the table moved. From this signal, an attenuation curve was obtained. Using a custom optimization algorithm, a reference spectrum generated with SpekPy [49] was iteratively adjusted by adding aluminium filtration until it matched the measured attenuation characteristics.

The spatial distribution is influenced by the bowtie filter of the CT and the collimators. **Figure 4** shows a systematic drawing of the collimation setup. The collimation width c is chosen by the operator. The bowtie filter can be described by an angular dependent thickness $d(\theta)$ calculated from an angular dependent attenuation $f(\theta)$.

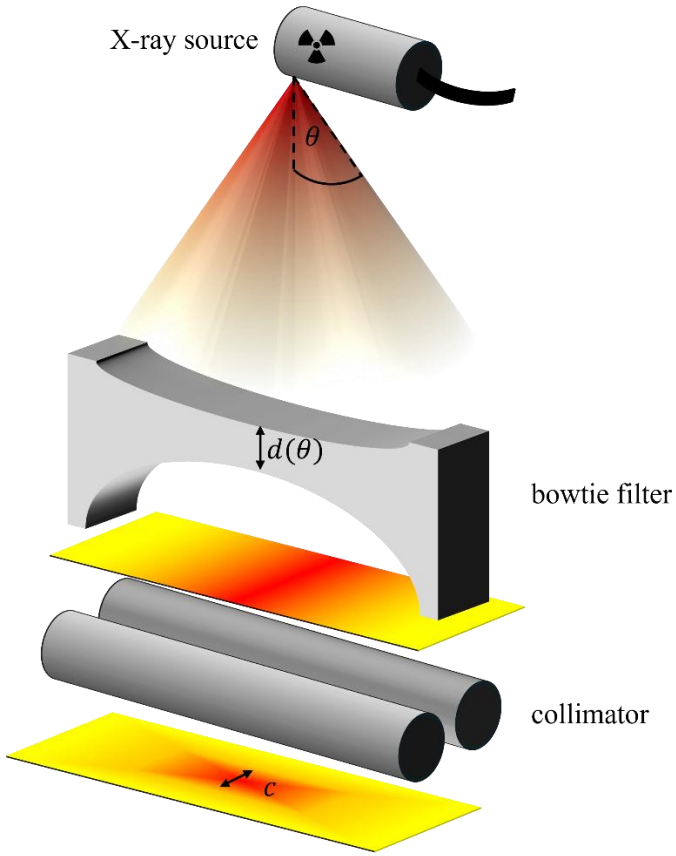

Figure 4. Schematic drawing of the collimation system of a CT scanner including the X-ray source, the bowtie filter with fan angle θ dependent thickness $d(\theta)$ and the collimator with collimation width c. The figure also shows the effect of the bowtie filter and collimator on the radiation field intensity (red: high intensity, yellow: low intensity).

To characterize the filtration properties of the bowtie filter, the COBRA methodology (Characterization of Bowtie Relative Attenuation) was employed, following Boone [50]. This approach allows for the determination of the spatially varying filtration introduced by bowtie filters. The experimental setup involved placing a Radcal RC0.6 ionisation chamber 25 cm

away from the isocentre, positioned outside the central axis of the gantry, as depicted in **Figure 3**, but without additional filtration. During data acquisition, the X-ray tube was continuously rotated while the chamber recorded time-resolved signals corresponding to different angular positions of the beam. This procedure resulted in a detailed attenuation curve as a function of angle, $f(\theta)$.

Using the X-ray spectrum previously derived from aluminium attenuation measurements, an angularly dependent aluminium-equivalent thickness profile of the bowtie filter was computed. This was achieved by calculating the additional aluminium thickness to fit the measured air kerma attenuation curve, using the method described by Rosendahl et. al. 2019 [47].

One example of the resulting aluminium equivalent source model can be displayed by the three plots in **Figure 5**.

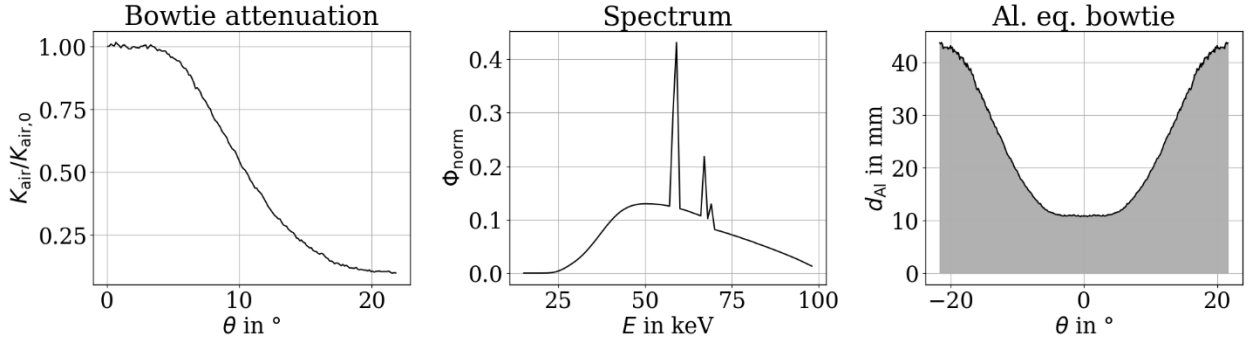

Figure 5. Example of a dataset describing the aluminium equivalent source model, left: measured relative angle dependent bowtie air kerma attenuation, middle: aluminium equivalent photon spectrum, right: calculated angle dependent aluminium equivalent bowtie filter thickness.

2.4.2 Implementation of the Particle Source

To define a new particle source for the C++ library of EGSnrc, the sampling of two particle properties must be implemented: direction $\vec{d}$ and energy E_{ph}.

The direction vector

$$\vec{d} = \frac{\vec{x}}{|\vec{x}|} = \frac{1}{|\vec{x}|}\begin{pmatrix}\tan(\theta)\\ \tan(\alpha)\\ 1\end{pmatrix}, \tag{19}$$

is characterized by two angles θ, which represents the angle in the xz-plane and α corresponds to the angle in the yz-plane, as illustrated in **Figure 6**.

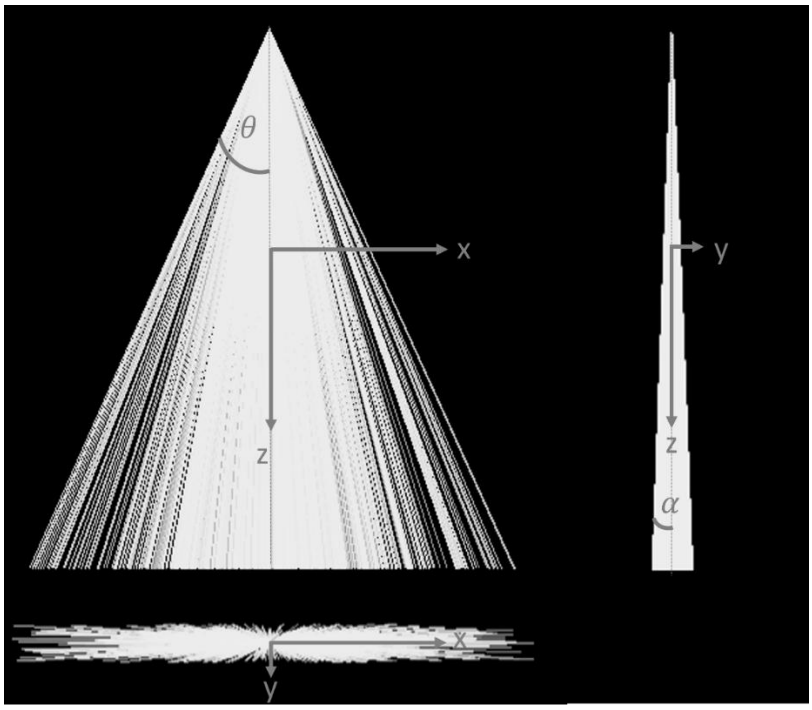

Figure 6. Example of photon track output of the implemented aluminium equivalent CT source and spatial orientation, from [1], Licensed under CC BY 4.0 (https://creativecommons.org/licenses/by/4.0/).

The sampling of θ was based on the relative kerma attenuation $f(\theta)$ of the bowtie filter, which was used as a PDF for the fan angle θ.

To perform sampling, the inversion method as described in 2.3.2 was employed, solving the equation:

$$\theta = F_\theta^{-1}(r), \tag{20}$$

where r is a random number uniformly distributed in [0,1] and F_θ^{-1} denotes the inverse CDF $F_\theta = \int f(\theta)$. To facilitate numerical inversion, the distribution was first smoothed using a convolution-based approach, followed by linear interpolation. Numerical integration was carried out using the trapezium rule [51]. Finally, the value of θ was obtained by solving equation (20) as a root-finding problem using Brent's method [52].

The angle α was sampled from a uniform distribution $[-\alpha_{\max}, \alpha_{\max}]$, constrained by the collimation in the *z*-direction. For this the maximal angle

$$\alpha_{max} = \tan^{-1}\left(\frac{c}{2}\Big/ d_{\mathrm{sc}}\right) \tag{21}$$

was calculated from the collimation c and the source-gantry-centre-distance d_{sc}.

In a second refined implementation, the build in sampling function of EGSnrc was used for the fan angle distribution sampling, using the continuous sampling option, which is based on the alias sampling method explained in 2.3.2.

The energy sampling of a particle is based on the determined photon spectrum Φ_E in the centre of the gantry and the angular dependent aluminium equivalent thickness of the bowtie filter. For the sampled fan angle θ the corresponding aluminium thickness $d_{\mathrm{Al}}(\theta)$ is used to calculate an attenuated spectrum

$$\Phi_{E,\mathrm{filtered}}(E,\theta) = \Phi_E(E) \cdot e^{(-\mu_{\mathrm{Al}} \cdot \rho_{\mathrm{Al}} \cdot d_{\mathrm{Al}}(\theta))}, \tag{22}$$

using Beer-Lambert law, with the total attenuation coefficient of aluminium μ_{Al} and the aluminium density ρ_{Al}. The attenuation coefficients, including coherent scattering effects, were obtained from the linear interpolated XCOM database [43].

2.4.3 Validation of the Particle Source Implementation

To verify the method, the developed EGSnrc particle source class was applied to a CT scanner setup and simulated air kerma values were compared with experimental measurements and a detailed BEAMnrc [53] source simulation based on manufacturer information. Initially, source-specific features such as the bowtie filter attenuation and the X-ray spectra were validated.

Properties of the used CT scanner are described in 2.1. Measurements were performed at all four tube voltages, using a 40 mm collimation and the large body bowtie filter.

2.4.3.1 Monte Carlo Simulation of Air Kerma

For validation purpose air kerma values had to be simulated. For this purpose, the EGSnrc C++ user code cavity was used. The data post-processing and analysis were performed using Python 3 (version 2.8.13). The transport parameters used are listed in **Table 1**.

To replicate the axial scan acquisition in the simulations, the particle source was rotated and shifted to reproduce the physical scan trajectory of the CT scanner's X-ray source. A separate MC simulation was performed for each discrete source position. An angular step of 1 ° was used for the rotation.

Table 1. Monte Carlo transport parameter for particle source validation simulations, from [1].

Parameter	Description
Code	EGSnrc release version 2020 [39]
Timing	PTB computing cluster (CPU), approx. 10^7 - 10^8 histories per hour depending on the geometry
Cross-sections	mcdf-xcom [43]
Transport parameters	electron cutoff 0.512 MeV (includes rest energy) photon cutoff 0.001 MeV
Variance reduction	none
Number of histories	10^8 - 10^{10} histories per simulation
Scored quantities	fluence, deposited energy
Statistical uncertainty	≤ 0.1 %
Postprocessing	Conversion of scored quantities to air kerma Normalization

For the validation of the bowtie attenuation the photon fluence with respect to energy $\Phi_E(E)$ was scored. The air kerma was calculated

$$K_{\mathrm{air}} = \sum_{E_{\mathrm{min}}}^{E_{\mathrm{max}}} \Phi_E(E) \cdot E \ . {\mu_{tr}(E)}/{\rho}. \tag{23}$$

using the mass energy-transfer coefficients ${\mu_{tr}(E)}/{\rho}$ for air. The coefficients were simulated with the EGSnrc usercode g [54].

For all the other simulations the air kerma $K_{\mathrm{air}} = \frac{E_{\mathrm{dep}}}{m}$ was determined as the quotient of the deposited energy E_{dep} and the mass m of the scoring volume. For the energy range of X-rays, this is a sufficient approximation, due to short electron range.

2.4.3.2 Validation against BEAMnrc CT Model

For the simulation of the realistic CT scanner source geometry the simulation tool BEAMnrc [55] was used. The source geometry was modelled using component modules, listed in **Table *2***. The schematic drawing of the different components is shown in **Figure 7**.

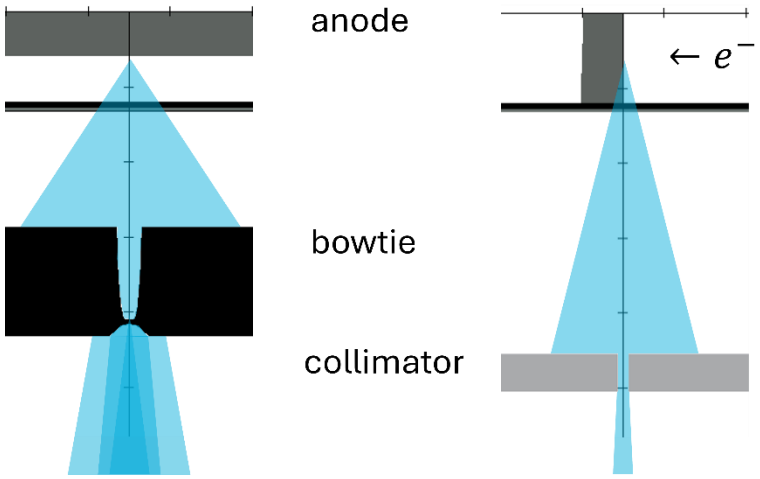

Figure 7. Schematic drawing of an example CT source geometry in BEAMnrc. left: Front view, right: Side view.

The geometry information was based on manufacturer information. In contrast to the image shown a photon spectrum calculated with the python module SpekPy [49], a validated software tool for the calculation of X-ray spectra, was used as input instead of the anode with an electron beam. This decision was made to speed up the simulation. As source ISOURC=1 was used, an isotropic point source, with the defined photon spectrum.

Table 2. Used component modules for different CT source components.

component	component module
Filtration	SLABS
Bowtie	JAWS
Collimators	JAWS

To save later calculation time phasespace files of the BEAMnrc source output were calculated, using 10^8 photons each. For each tube voltage 1000 phase space files were generated and randomly chosen during following simulations to avoid correlations.

The new implemented source was compared to the BEAMnrc source for the aluminium attenuation curve and the bowtie profiles, presented in section 3.1.1.

2.4.3.3 Table Density Estimation

The scanner included a carbon-fibre-reinforced plastic patient table, which served to support the experimental setup and is referred to as the patient table in this manuscript.

The patient table significantly attenuates the photon radiation and therefore must be considered when comparing measurements and simulations. The composition of the table material and thus the attenuation of the radiation, is normally unknown. To overcome this problem, a semi-empirical method for modelling the patient table was developed as described in [1]. The method is based on a comparison of MC simulation results and dose measurements.

To characterize the attenuation caused by the patient table, the ratio of the air kerma at the bottom position $K_{\mathrm{exp}}(\mathrm{p6})$ of a PMMA CTDI body phantom, which is more strongly affected by the table attenuation, to the air kerma at the top of the phantom $K_{\mathrm{exp}}(\mathrm{p12})$, which experiences less attenuation, was evaluated (**Figure 8**). The ratio is defined as

$$\kappa_{\mathrm{exp}} = {K_{\mathrm{exp}}(\mathrm{p6})}\Big/{K_{\mathrm{exp}}(\mathrm{p12})}\,. \tag{24}$$

The CTDI phantom consists of a 15 cm long PMMA cylinder with a 32 cm diameter and has five holes for placing an ionisation chamber—four on the periphery and one at the centre.

For the material definition in the Monte Carlo simulation a composition of 40 % epoxy resin and 60 % carbon fibres were assumed [56]. Based on the chemical composition of epoxy resin from [57], the elemental composition of the patient table material was defined as 68 % carbon, 27 % hydrogen and 5 % oxygen. The volume fraction, the mass fractions, the densities and chemical compositions of the two components are presented in table **Table 3**.

Table 3. Material composition of the CT scanner table: volume fraction, density, mass fraction and chemical composition of the two components, from [1].

Material	Volume fraction (%)	Density ($g \cdot cm^{-3}$)	Mass fraction (%)	Chemical composition
Carbon fibre	60	1.80	68	C
Epoxy	40	1.25	32	$C_{12}H_{16}O_4(C_{18}H_{20}O_3)_{2n}$

The simulations were carried out with an identical CTDI-phantom setup for a range of different densities ρ between 1.5 g cm^{-3} and 3.5 g cm^{-3} of the patient table modelled from carbon fiber reinforced plastic. For the resulting density dependent simulated attenuation values

$$\kappa_{\mathrm{MC}}(\rho) = {K_{\mathrm{MC}}(\mathrm{p6})}\Big/{K_{\mathrm{MC}}(\mathrm{p12})} = a \cdot \rho + b\,, \tag{25}$$

a linear relationship was seen in the data. Therefore, a linear fit was calculated, with the fitting parameters a and b. The material density corresponding to the experimental values can be determined using the following equation:

$$\rho_{Table,MC} = \frac{1}{a}\left(\kappa_{\exp} - b\right). \tag{26}$$

For the uncertainty estimation the values from the covariance matrices were used.

To further verify the table's density, primary photon attenuation was measured at the centre of the gantry using a Farmer-type ionisation chamber. A time-resolved measurement curve was recorded during a complete rotation of the X-ray tube around the chamber, and this curve was replicated using the determined table density in the simulation.

2.4.3.4 Phantom Measurements and Simulation

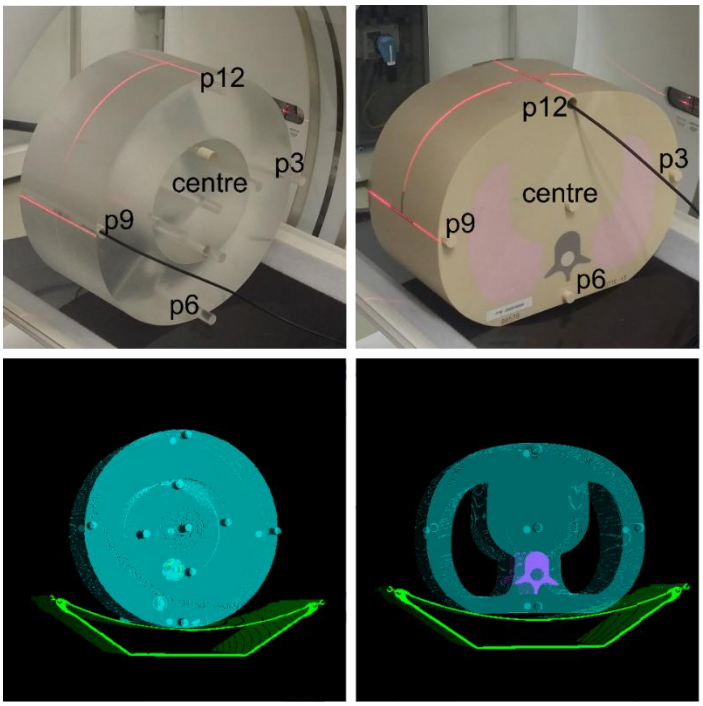

Figure 8. Measurement set-ups of the phantom measurements at the GE OptimaCT 660 with marked measurement positions (top). Simulation geometries of the two phantoms (bottom). CTDI phantom (left) and thorax phantom (right). from [1], Licensed under CC BY 4.0 (https://creativecommons.org/licenses/by/4.0/).

The X-ray spectra and bowtie attenuation were measured as previously described in 2.4.1.

Additional validation was carried out using two phantoms: a CTDI phantom (PTW, Freiburg, Germany) and a thorax phantom (CIRS, USA). The simulation and measurement geometries are shown in **Figure 8**.

The anthropomorphic thorax phantom, mimics human anatomy using three materials representing soft tissue, lung and bone. It also has five equivalent measurement positions (see **Figure 8**).

Measurements were taken at each of the possible positions in both phantoms, with the remaining holes filled using matching material rods. Scans were conducted in axial mode using a single rotation, a 2-second rotation time and a tube current of 100 mA. The centre of each phantom was aligned with the CT scanner's isocentre.

For the comparison between measurement and simulation results a conversion factor $k_{N,Q}$ between time current product Q at the CT scanner and number of particles N in the simulation was needed. The conversion factor was calculated by

$$k_{N,Q} = \frac{K_{\mathrm{exp,ref}}}{Q} \frac{N}{K_{\mathrm{MC,ref}}}, \tag{27}$$

with $\frac{K_{\mathrm{exp,ref}}}{Q}$ measured with an RC0.6 Framer chamber free in air in the centre of the CT gantry and $\frac{K_{\mathrm{MC,ref}}}{N}$ simulated at the same position.

To ensure the linearity between measured value and time current product, measurements were performed for each tube voltage and eight current values from 50 mA to 400 mA.

2.4.4 Uncertainty Estimation

The uncertainty evaluation follows the guidelines outlined in JCGM 100:2008 [34]. The air kerma estimated from MC simulations is calculated using the following model equation:

$$K_{\mathrm{MC}} = k_{N,Q} \cdot \frac{K_{\mathrm{sim}}}{N} \cdot Q \cdot k_{\mathrm{SPEC}} \cdot k_{\mathrm{BT}} \cdot k_{\mathrm{PT}} \cdot k_{M}. \tag{28}$$

Equation (28) defines how the simulated air kerma value K_{MC} is estimated for a given current-time product Q. The factor $k_{N,Q}$ converts the MC simulation result $\frac{K_{\mathrm{sim}}}{N}$, which is normalized per particle N, into a value normalized by the CT scanner's operational parameter Q.

Several correction factors are included to account for additional influencing parameters:

- k_{SPEC}: spectrum correction
- k_{M}: material definition
- k_{BT}: bowtie filter shape
- k_{PT}: patient table density

The uncertainties associated with these factors, denoted σ_{i}, are summarized in the results in **Table 11** in section 3.1.4. For measured air kerma values, uncertainty was evaluated both for in-air measurements and those conducted with phantoms. When using the RC0.6 Farmer-type ionisation chamber in free air, a combined standard uncertainty ($\sigma_{\mathrm{c,exp}}$) of 0.72 % (with a coverage factor ($k = 1$)) was determined. The full uncertainty budget is detailed in **Table 12** in section 3.1.4. This measurement uncertainty contributed most significantly to the overall uncertainty in the normalization factor $k_{N,Q}$.

To assess the uncertainty in the simulation, a sensitivity analysis was conducted on the various contributing factors. For the material correction factor k_M, the PMMA density was varied between $1.17\ \mathrm{g/cm^3}$ and $1.19\ \mathrm{g/cm^3}$. These boundaries were chosen based on literature data (material data EGSnrc, [57]) and the measurements of 7 PMMA probes at the PTB (**Table 16**). For the patient table correction k_{PT}, uncertainty in the material density was derived from the linear regression described in Equation (25), with propagation of uncertainty applied to the value calculated using Equation (26). This resulted in a density range of $1.88\ \mathrm{g/cm^3}$ to $2.43\ \frac{\mathrm{g}}{\mathrm{cm^3}}$. The corresponding effect on the simulated air kerma was used to estimate uncertainty, assuming a rectangular distribution.

As the same experimental approach was used as in [47] and the uncertainty related to the bowtie filter shape had already been assessed in that prior study, no new sensitivity analysis was conducted for k_{BT}; the previously determined uncertainty value was adopted.

The statistical uncertainty of the simulated value K_{sim} was taken directly from the MC simulation output.

To evaluate uncertainty in the X-ray spectra, additional simulations were carried out using the CTDI phantom and two alternative spectra with different mean energies, as shown in **Figure 9**. The lower-energy spectrum was generated using the SpekPy Python module [49], based on the specified tube voltage, anode angle and filter materials provided by the manufacturer. For the higher-energy spectrum, an extra aluminium filter was added to achieve an equivalent mean energy shift in the opposite direction.

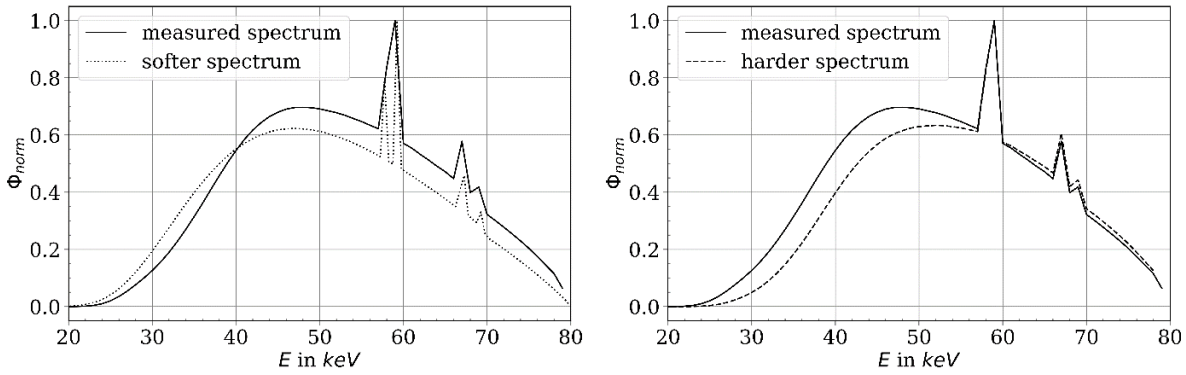

(a) Softer spectrum $E_{\text{mean}} = 50.84\ keV$ (b) Harder spectrum $E_{\text{mean}} = 54.78\ keV$

Figure 9. Illustration of the spectra used for uncertainty estimation for the X-ray spectrum dependency of the simulated air kerma results, from [1], Licensed under CC BY 4.0 (https://creativecommons.org/licenses/by/4.0/).

2.5 Machine Learning for Dose Calculation

This chapter discusses selected principles of machine learning, as presented in [59]. Machine learning refers to computational models that are able to adjust based on data.

There are different types of ML algorithms, for example, neural networks, decision trees, supported vector machines and Bayes networks. In this work, only neural networks were used, hence this chapter will focus on those. Neural networks (NN) belong to the ML subfield of deep learning.

2.5.1 Neural Networks

The simplest type of neural network is the fully connected neural network (FCNN). An example of the structure of a FCNN is shown in **Figure 10**.

The term "fully connected" denotes that every neuron in a layer is connected to every neuron in the subsequent. In the input layer, the input feature vector X_0 is entered into the NN. The values of layer n are calculated by

$$X_n = \sigma(W_n \cdot X_{n-1} + b_n), \tag{29}$$

with the weight matrix W_n, bias vector b_n and the non-linear activation function σ. The layers between input and output layer are called hidden layer.

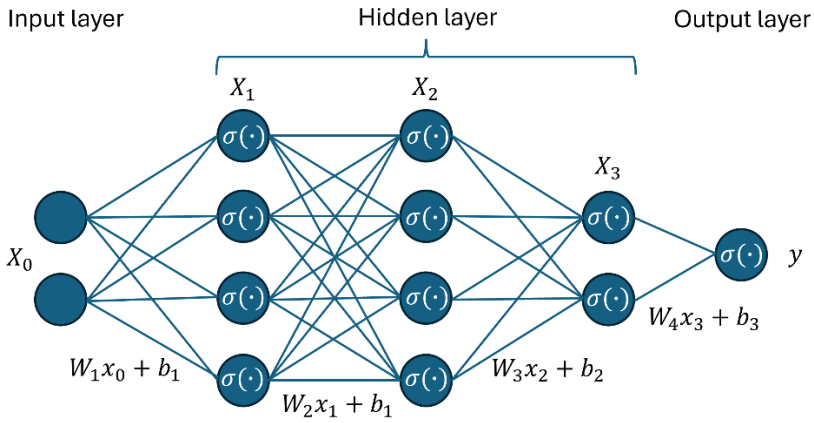

Figure 10. Schematic drawing of a fully connected neural network. The network consists of an input layer, two hidden layers, in which each neuron applies a activation function σ, and an output layer.

The training of a neural network is the adjustment of the weights according to the provided data. The neural network output y is compared to the ground truth y' by evaluating a loss function L(y, y'). An example loss function is mean-squared-error $MSE = \frac{1}{n}\sum_{i=0}^{n}(y_i - y_i')^2$. Based on such a function the networks' weights are adjusted to minimize the loss function. For the minimizing process an optimization algorithm is used.

The convolutional neural network (CNN) is a specific type of neural network. It employs convolutions to extract features from multidimensional data. The convolution matrices represent the weights that are applied to the input data. The primary benefit of CNNs is their ability to significantly reduce the number of weights needed for processing multidimensional data compared to FCNNs. One special form of CNN is the so-called U-Net. Developed by Ronnenberger, et. al. [60] it is very efficient in several imaging-based tasks. The name is based on its shape, as shown in **Figure 11**. In the contracting downward path (encoder), the input is analysed (convolutions) and down-sampled (pooling) and the key components of the input are determined. In the expanding path (decoder), this information is refined to the original size by applying up-convolutions. In addition, localization information is provided by cross-connection between the down and upward paths.

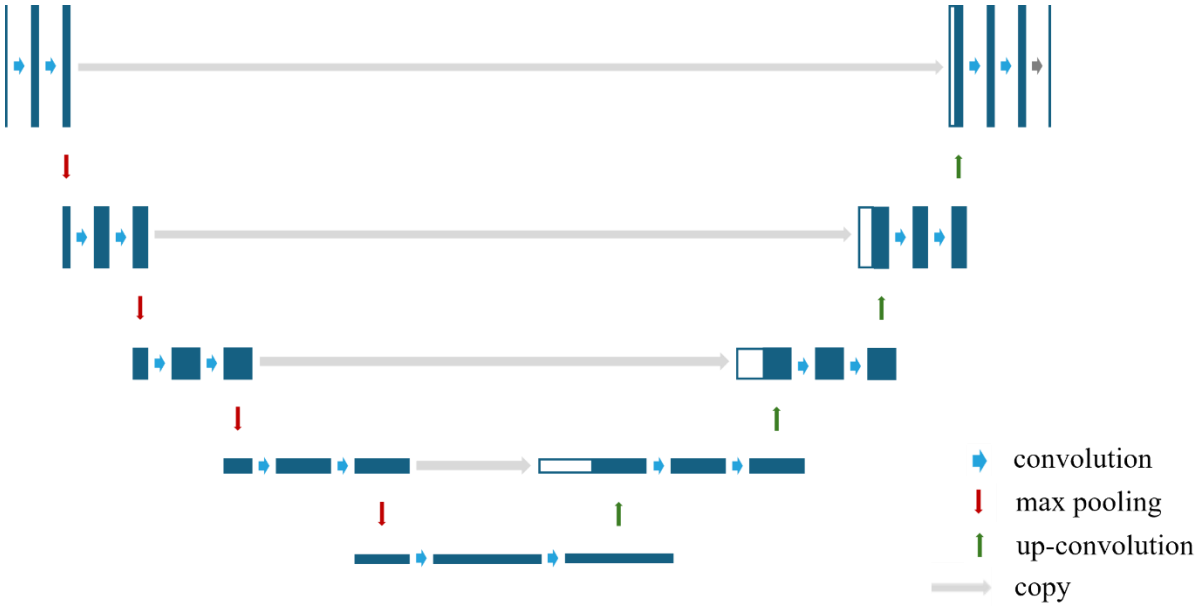

Figure 11. Schematic drawing of a U-Net Structure, with the arrows describing mathematical operations. Blue arrows: convolution, red: max pooling, green: up-convolution, grey: cross-connections.

The network architecture used in this work was a 3D-U-Net with a depth of four, as shown in **Figure 11**. For each step in the encoder path a convolutional block is applied, consisting of two convolutions (blue arrows) with a kernel size of 2x2x2, each combined with a batch normalization. The used activation function was ReLu (rectified linear unit). The down sampling was achieved by applying max-pooling layers (red arrows), also with a kernel size of 2x2x2. The decoder path was constructed similarly, using 2x2x2 transposed convolution kernels (green arrows). For the last layer a 1x1x1 convolution kernel was applied to get the output dose map.

2.5.2 Generation of Training Datasets

The neural network implemented in this work is supposed to calculate a 3D-dose distribution. The dose prediction network gets two input features as presented in **Figure 12**. The first is an electron density map of the patient geometry to provide geometrical information. The second input provides the radiation field information by presenting an 3D-air kerma attenuation curve in a water cylinder. The network output is a 3D-dose map of the patient geometry. For the ground truth training data, MC simulated dose distributions were used.

Anatomically realistic human body models serve as the foundation for generating these data. The following sections describe the datasets used, including synthetic phantoms and real patient data, followed by the generation of network inputs and target dose values through simulations and data preprocessing.

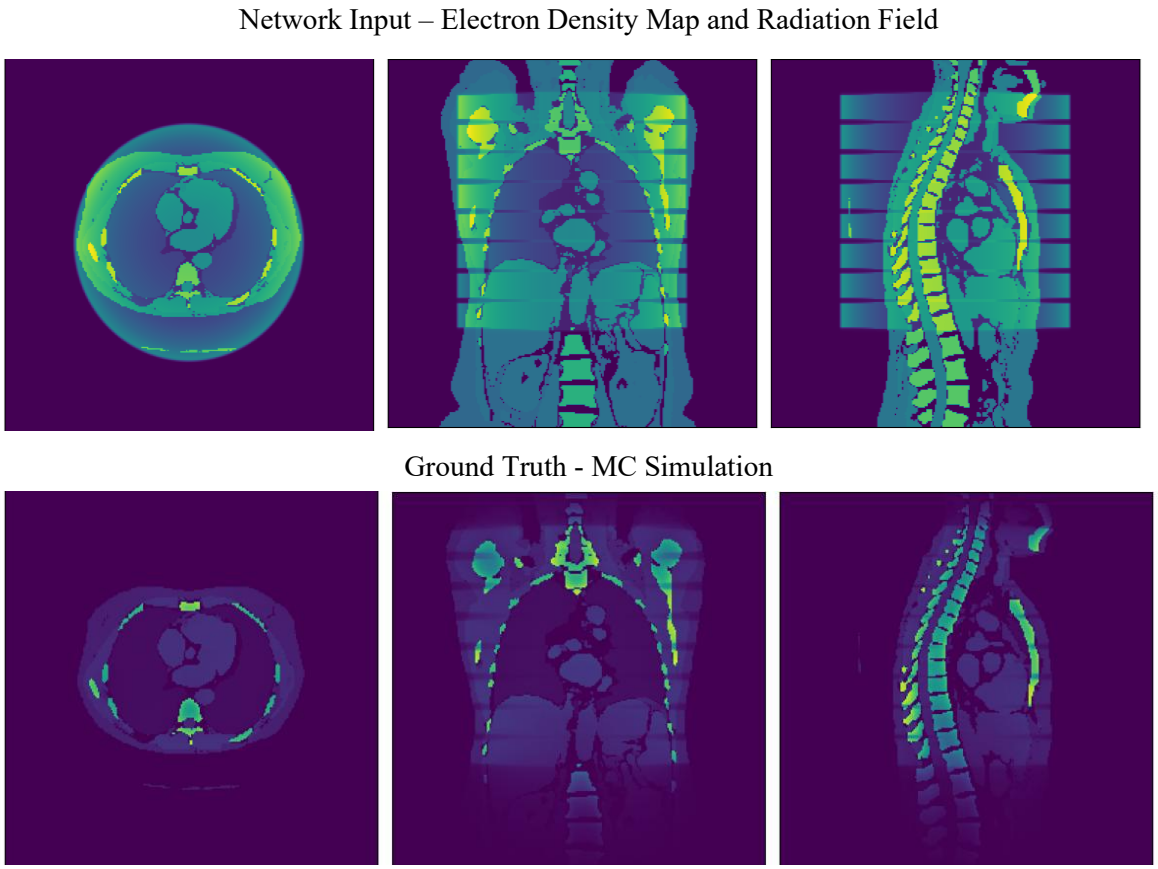

Figure 12. Example network inputs and ground truth MC data. Top: Electron density map overlaid with the radiation field characterization map. Bottom: MC ground truth data.

2.5.2.1 Virtual Phantom Dataset

To create realistic virtual patients for simulation purposes, XCAT version 2 software [61] developed at Duke University was used to create human body phantoms. The aim was to create a population of virtual patients with a variety of body sizes and organ volumes. The XCAT software required several input parameters including organ volumes, fat layer thickness and body height to define each phantom. The complete list of parameters is presented in **Table 4**. To achieve a diverse data set, the values were sampled from uniform distributions with defined boundaries.

Patient body heights were sampled from a uniform distribution ranging from 1.50 m to 2.10 m, covering the expected range for adult males and females. The generation of organ volumes was based on reference data from ICRP Publication 145 [62]. For each organ, values were sampled from a uniform distribution centred around the mean reported in the ICRP data, with a ±10 % range applied.

To account for differences in body composition, different scaling factors were used. These factors, sampled from the range [0.90, 1.10]. A single fat layer scaling factor was applied consistently across all regions of each phantom to maintain anatomical proportionality.

For each parameter, 200 values were generated and random combinations of these were used to create 200 synthetic adult phantoms—comprising 100 female and 100 male models. Three example phantoms from the dataset are shown in **Figure 13**.

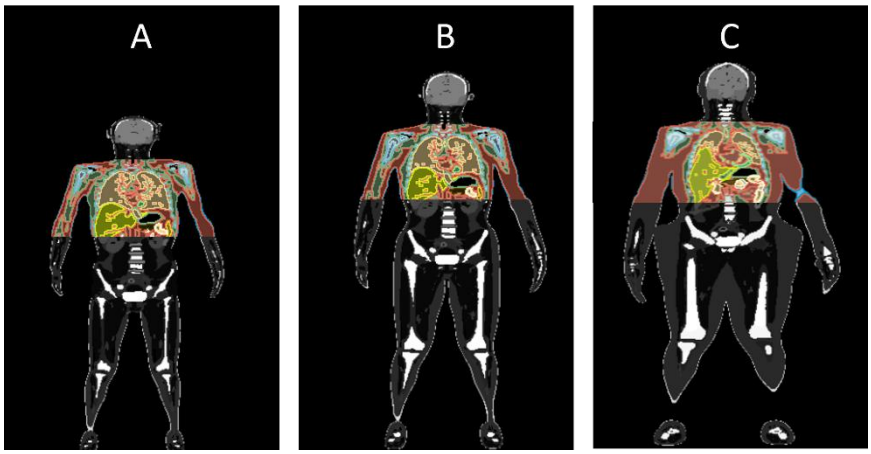

Figure 13. Example of three phantoms from the generated phantom dataset, each representing a different body shape. The coloured regions indicate the simulated scan areas, along with the segmented organs used for effective dose calculation, from [2].

Table 4. Input parameter for XCAT phantom generation: Mean values for organ volumes and list of scaling factors, each with a range of [0.90, 1.10].

parameter	mean value [62] Organ volumes in cm^3		Scaling factors
	male	female	
prostate	17.1		phantom_height_scale
testes	35.8		hrt_scale_x
liver	2234.9	1707.5	hrt_scale_y
stomach	427.6	387.8	hrt_scale_z
pancreas	166.3	138.6	lung_scale
spleen	215.5	176.8	head_height_scale
gall bladder	66.3	54.5	head_skin_x_scale
right kidney	203.0	154.8	head_skin_y_scale

left kidney	197.9	184.4	chest_skin_long_axis_scale
right adrenal	8.4	8.4	chest_skin_short_axis_scale
left adrenal	8.4	6.6	abdomen_skin_long_axis_scale
small intestine	1172.3	1004.1	abdomen_skin_short_axis_scale
large intestine	764.7	743.5	pelvis_skin_long_axis_scale
bladder	241.4	231.5	pelvis_skin_short_axis_scale
right thyroid lobe	11.1	9.3	arms_cir_scale
left thyroid lobe	11.1	9.3	arms_length_scale
thymus	25.1	19.9	arms_skin_cir_scale
salivary	85.4	69.6	legs_cir_scale
pituitary	0.6	0.6	legs_length_scale
eyes	15.1	15.1	legs_skin_cir_scale
right ovary		6.0	bones_scale
left ovary		6.0	
ftubes		2.1	
uterus		80.3	
larynx	27.2	18.4	
trachea	10.1	8.0	
esophagus	72.0	62.2	
epidy	3.8		
right breast	13.2	261.5	
left breast	13.2	261.5	
breast glandular	10.1	200.8	
breast adipose	16.3	322.8	
brain	1457.6	1296.4	
heart tissue	367.1	276.8	

To assess the dosimetric behaviour across the dataset, a small simulation study was conducted by the PhD-candidate and presented in [2], using the three example phantoms: one corresponding to ab average adult, and two representing anatomical extremes. In the study the organ based effective dose and the effectives doses based on CTDI and SSDE as described in section 2.2.1 were simulated. For the simulation the previously presented particle source was used. The simulation was performed for a typical lung scan between the cervical vertebrae and adrenal gland [63].

2.5.2.2 Real Patient Dataset

The synthetic dataset was complemented with 116 anonymized whole-body CT scans obtained from Klinikum Braunschweig, comprising scans from 54 female and 62 male adult patients. Using the TotalSegmentator software [64], the CT scans were segmented into 104 distinct organs and tissues. For the purposes of simulation, several of these tissues and organs were grouped together (see Table 5).

Although the original data encompassed the entire body, this study focused solely on the thoracic region. To isolate this area, an automated region-of-interest (ROI) extraction was performed using anatomical landmarks, capturing slices from the cervical vertebrae down to the adrenal glands. An additional 30 slices were included at both the upper and lower boundaries.

2.5.2.3 Training Data Set Generation and Preprocessing Steps

As ground truth data MC simulated dose distributions were calculated using the particle source described in section 2.4.

Table 5. Material definition parameters for radiation transport simulation for training data generation.

material	density in g/cm^3	electron density in $m^{-3} \cdot 10^{26}$ [65]	density correction file
Air	0.0012	3.3	air_dry_nearsealevel
Muscle	1.04	3480	muscle_skeletal_icrp
Lung	0.27	862	lung_inflated_icru_1986
Spine Bone	1.85	5950	bone_cortical_icrp
Rib Bonde	1.85	5950	bone_compact_icru
Fat	0.92	3180	adiposetissue_icrp
Blood	1.06	3510	blood_icrp
Heart	1.06	3510	heart_blood-filled_icru_1986
Kidney	1.05	3480	kidney_icru_1986
Liver	1.06	3510	liver_icru_1986
Pancreas	1.04	3460	pancreas_icru_1986
Intestine	1.03	3420	gitract_intestine_icru_1986
Scull	1.85	5950	bone_compact_icru
Brain	1.03	3460	brain_icrp
Spleen	1.06	3510	spleen_icru_1986

For the source parameters 120 kV and a 40 mm collimation were chosen. For every anatomy eight axial source positions along the scan axis were simulated. Beforehand all data was resampled to the same resolution of 3mm x 3mm x 4mm. For the simulation the same MC parameters were chosen as presented in **Table 1** only differing in scored quantity, which was the dose per particle for each voxel saved in a .3ddose file for the phantom simulations.

Two inputs were used for the neural network as illustrated in **Figure 12**. The segmented patient geometries were converted to electron density distribution, to represent the radiation interaction properties of the tissue. For the conversion the electron densities from the ICRU Report 46 [65] were used.

Radiation field input

As input to characterize the radiation field an air kerma attenuation of the CT radiation field was calculated using a ray tracing algorithm based on the software implemented by Lehner et.al. [66].

First, a direction is sampled in given boundaries, and a ray is traced along with the given orientation. During this process, the materials of the traversed voxels are identified. Next, the water equivalent distance d is calculated based on the voxel dimension. This distance is used to determine the kerma. The kerma K in water distance d is calculated by

$$K(d) = \sum_E \left(\Phi(E) * e^{-\mu_W(E)\cdot\rho_W\cdot d}\right) \cdot E \cdot \mu_{tr,A}(E) \cdot \Delta E, \qquad (30)$$

with the discrete photon fluence $\Phi(E)$ exponential attenuated by the given thickness of water, the mass energy transfer coefficient of air $\mu_{tr,A}$, summed over the spectral energies E and bin width ΔE of $\Phi(E)$.

Finally, the corresponding value is set and weighted by the angular probability w given by the measured bowtie filter attenuation and attenuated using the distance-square-law. To reduce computation time, the resulting kerma value map is rotated and translated to mimic the CT source positions and their respective dose contributions.

An example of the three-dimensional attenuation is shown in **Figure 14**.

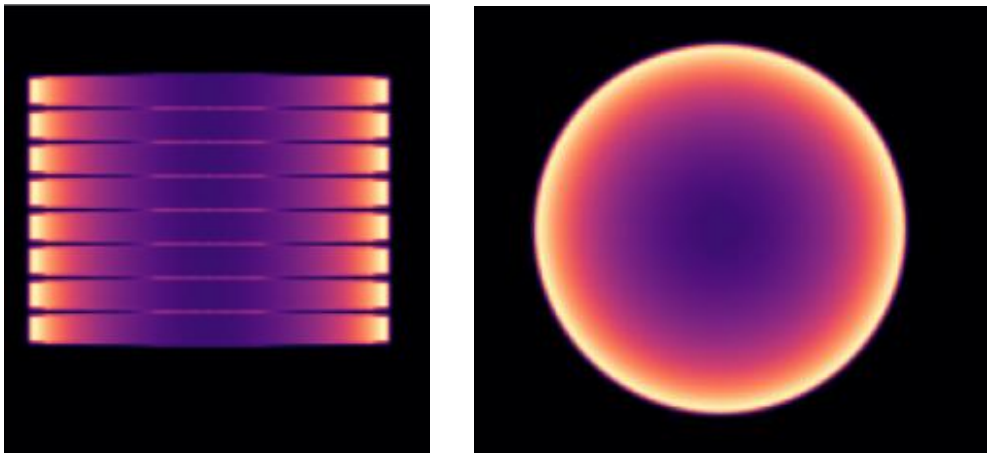

Figure 14. Example of a three-dimensional attenuation curve for a CT scan in a water cylinder with a diameter of 32 cm. left: z-x view, right: x-y view.

Data preprocessing

To prepare the data for training of the neural network, the data was pre-processed to ensure fast data loading during training. As a first step began random points were selected within the body volume of each patient or phantom. Sampling was restricted to anatomically relevant regions, ensuring underrepresentation of air voxels in the training data.

For each position, a three-dimensional patch with a size of 32×32×32 voxels were extracted from both the input data and the corresponding dose distribution from MC simulations. An example is shown in **Figure 15**.

Figure 15. 2D-representation of patch sampling from a phantom geometry. Patch centre points were sampled inside the phantom geometry and 32x32x32 patches were extracted around the centre point.

To ensure numerical stability, all input and output data were normalized to the range [0,1]. Normalization was performed globally for the entire data set using fixed scaling parameters derived from the expected maximum values of each variable.

After normalization, the dataset was split into non-overlapping subsets for training and validation. A test dataset consisting only of real patient data from 28 patients was taken out beforehand.

The processed data were serialized and stored as Python pickle files.

2.5.3 Network Training

In the development process, in a first step a dose prediction network was trained, whose only output was a dose map $\mu(x)$. In a second step the network output dimension and the loss function were modified to account also for uncertainty estimation as described in section 2.5.4. The training procedure was the same for both networks.

The neural network was trained to determine a 3D map of continuous dose values for each voxel x. The loss function was defined as a voxel wise mean squared error

$$\mathcal{L}_{MSE} = \frac{1}{n}\sum_{x=1}^{n}(\mu(x) - D(x))^2 \cdot M(x), \tag{31}$$

between the neural network prediction $\mu(x)$ and the ground truth values $D(x)$.

To focus the training on relevant areas, a binary mask M was used that only considers voxels that belong to the patient's body volume. This mask was created based on the segmentation of the patient's body and applied to the loss during training so that only the masked voxels were used to calculate the gradient. This serves to avoids unnecessary optimization outside the body.

The Adam optimizer was used as the optimization algorithm. The initial learning rate was set to 0.001. The training was performed over 1000 epochs, which took depending on training dataset size roughly 24 h. Model checkpoints were saved at intervals of 100 epochs to later select the optimal working network and detect overfitting.

For the training a computer unit with an NVIDIA RTX A5000 GPU (24 GB VRAM), an Intel Core i9-14900K processor, 128 GB DDR5 RAM and the Windows 11 Pro operating system was used. The implementation was carried out with PyTorch version 2.3.1, using CUDA 12.1 for GPU acceleration. The training pipeline was developed entirely in Python.

2.5.4 Uncertainties of a Neural Network

In a second step the network output and the loss function was adapted to account for uncertainty evaluation. For the uncertainty analysis the approach presented in [67] by Lakshminarayanan et al. was adapted, analysing two sperate uncertainty aspects: the uncertainties rooted in the training data (aleatoric uncertainty) and the uncertainties from the model training (epistemic uncertainty). A central component of the method proposed by Lakshminarayanan et al. was the training of an ensemble of neural networks, where each model is initialized with different random weights and trained independently. Different initializations and different orders of the training data can lead to convergence to different local minima. As a result, each network in the ensemble learns a different function, even when trained on the same dataset. This diversity among ensemble members is crucial for capturing epistemic uncertainty, which reflects the uncertainty of the model about its own parameters due to limited data. During inference, the predictions of all nets $\mu_i(x)$ are averaged to obtain a final output distribution. For the epistemic uncertainty the variance

$$\sigma^2_{\text{epistemic}}(x) = \frac{1}{5}\sum_{i=1}^{5}(\mu_i(x) - D(x))^2 \tag{32}$$

over the five trained networks was used.

The selection of an appropriate loss function is essential in training neural networks for the estimation of the aleatoric uncertainty. In this work the negative log-likelihood was used as loss function. For the loss function it was assumed to model an output $y \in \mathbb{R}^D$ as a Gaussian distribution with a mean $\mu(x)$ and a variance $\sigma^2(x)$ for each voxel x. The negative log-likelihood of a heteroscedastic Gaussian model is given by

$$\mathcal{L}(x) = \frac{1}{2}\exp\left(-\log\tilde{\sigma}^2(x)\right)\big(y(x) - \mu(x)\big)^2 + \frac{1}{2}\log\tilde{\sigma}^2(x) \tag{33}$$

which was used as the loss function of the training. This function ensured that the model predicts a distribution and not just a point estimate, which was realized by two output layers, which presented the mean and the logarithmic variance for each voxel. The function was minimized when the predicted distribution matched the ground truth distribution. The loss function penalized both inaccurate mean estimates and an inadequate uncertainty estimate. It also prevented a trivial solution due to oversized variance values, as the logarithm of the variance is explicitly part of the cost function.

For the total loss

$$\mathcal{L}_{\text{total}} = \sum_{x} M(x)\mathcal{L}(x)\,. \tag{34}$$

The function from equation (33) was again multiplied with the binary mask, to only optimize on dose prediction inside the patient body.

To incorporate the uncertainty of the Monte Carlo ground truth data of 5.5 % (k=1) [1] it was added to the output values by

$$\log\,\tilde{\sigma}^2{}_i(x) = \log(\sigma^2{}_i(x) + \,(\mu_i(x) * 0.055)^2) \tag{35}$$

in the last layer of the network. The aleatoric uncertainty

$$\sigma^2_{\text{aleatoric}} = \frac{1}{5}\sum_{i=1}^{5}\tilde{\sigma}^2{}_i(x) \tag{36}$$

was than calculated as the mean value over all five ensemble networks.

The total uncertainty

$$\sigma_{total}(x) = \sqrt{\sigma^2_{\text{epistemic}}(x) + \sigma^2_{\text{aleatoric}}} \tag{37}$$

was calculated as the square root of the sum of the two variances.

For the organ doses, the uncertainty of each voxel was propagated to determine the individual organ dose uncertainties. To ensure scalability, the calculations assumed full correlation of uncertainties between voxels. This simplification was necessary because computing and storing the full covariance matrix for the large 3D dose maps, would require handling on the order of 10^{14} covariance terms, corresponding to several petabytes of data – making the computations expensive in both time and memory.

Under the assumption of full correlation, the variance of the mean can be expressed as

$$\sigma^2_{\text{organ}} = \frac{1}{{N_{\text{organ}}}^2}\sum_{i=1}^{N_{\text{organ}}}\sum_{j=1}^{N_{\text{organ}}}\sigma_{\text{tot}}(i)\sigma_{\text{tot}}(j) = \frac{1}{{N_{\text{organ}}}^2}\left(\sum_{i=1}^{N_{\text{organ}}}\sigma_{\text{tot}}(i)\right)^2, \tag{38}$$

with N_{organ}as the number of organ voxels.

2.5.5 Network Performance Evaluation

For the evaluation of the network performance, organ doses were calculated by applying the segmentation map to the estimated 3D dose distribution D. The organ doses were computed using the following equation:

$$D_{\text{organ}} = \frac{1}{N}\sum_i D_i \cdot M_{i,\text{organ}}\,, \tag{39}$$

where M_{organ} was a binary mask for each organ. The voxel dose values within each organ were summed and then divided by the number of voxels belonging to the organ.

The organ doses and summed organ doses were compared to the values obtained by MC simulations. The uncertainty values for the organ doses and the sum were calculated using uncertainty propagation of the voxel uncertainties, determined as described in 2.5.4.

2.5.6 Optimization of the used Training Data Set

The composition of training data plays a critical role in determining a neural network's ability to generalize and possible biases [68]. To address this issue, the utilization of synthetic training data has become a common practice in domains such as lesion classification [33] and image segmentation [34]. Russ et al. (2019) [69] demonstrated the feasibility of generating anatomically realistic CT images from XCAT phantoms using CycleGANs, showing enhancing performance of segmentation when synthetic and real data were integrated. In a similar vein, the study by Khosravi et al. (2024) demonstrated that augmenting datasets such as CheXpert and MIMIC-CXR with synthetic chest X-rays led to enhanced performance, with optimal gains observed at a synthetic-to-real ratio of approximately 10:1 [70].

Computational models like XCAT facilitate the generation of datasets exhibiting anatomical diversity, with controllable statistical properties.

Four neural networks, named according to the proportion of real patient data in their training datasets, were trained using different ratios of real to synthetic data: 0% NN (0% real / 100% synthetic), 10% NN (10% real / 90% synthetic), 20% NN (20% real / 80% synthetic) and 100% NN (100% real / 0% synthetic). Each data set was divided into 85% for training and 15% for validation. A separate, pre-defined test dataset - consisting exclusively of real patient data from 28 individuals - was used for evaluation. Only real patient data was selected for evaluation, as this is the data domain in which the network will ultimately operate.

3. Results

This chapter presents the results obtained throughout the development and evaluation of the dose estimation pipeline for personalised CT dosimetry. The findings are organized according to the key components of the workflow: validation of the CT particle source, dataset generation and performance analysis of the proposed U-Net-based dose prediction model. Each section presents quantitative evaluation and uncertainty discussions where applicable.

3.1 CT Particle Source

A customizable CT particle source was developed to simulate realistic photon fluences. This section presents the validation free in air, followed by the density estimation for the patient table material, air kerma evaluation in two phantoms and a detailed uncertainty analysis.

3.1.1 Free-Air Validation

To compare simulated and measured data conversion factors as described with equation (27) between time current product and simulated particle number was determined. The factors were measured for a current time product of $Q = I \cdot t = 100\ \text{mA} * 2\ \text{s} = 200\ \text{mAs}$. The conversion factors determined are listed in **Table 6**.

Table 6. Measured and simulated air kerma values and the resulting conversion factor to compare simulation and measurement results.

Tube voltage U in kV	$K_{\text{exp,ref}}/Q$ in $\text{Gy} \cdot \text{mAs}^{-1}$	$K_{MC,\text{ref}}/N$ in Gy per particle	$k_{N,Q}$ in mAs per particle
80	7.350E-05	3.972E-15	1.85054753E+10
100	1.335E-04	3.800E-15	3.51338668E+10
120	2.070E-04	2.729E-15	5.55144036E+10
140	2.927E-04	3.727E-15	7.85357668E+10

Figure 16 presents the measured air kerma values for various tube voltages as a function of the selected tube current, with tube rotation time held constant. The plot demonstrates a strong linear relationship, as indicated by the high R^2 values. Therefore, the conversion factors can be seen as valid for the whole current range of the CT scaled by the respective used tube current.

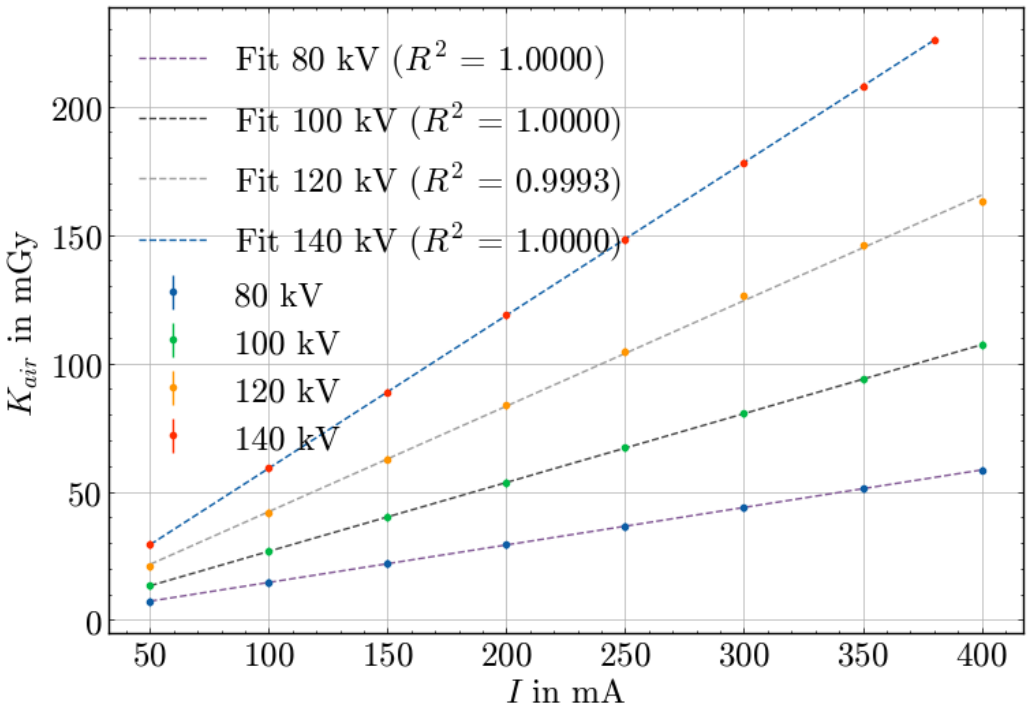

Figure 16. Measured air kerma values as a function of tube current for four different tube voltages, with constant tube rotation time. Error bars represent combined measurement uncertainty. Linear fits are shown as dashed lines, with corresponding R^2 values.

To validate the simulated photon fluence two aspects must be looked at: the energetic distribution and the spatial distribution of the x-ray photons. To characterize the energy distribution of the photons, an aluminium attenuation curve was determined by measurements and simulations. The results are presented in **Figure 17**. The experimental measurements are shown in black, the CT particle source simulations (al. eq. CT source) with blue stars and the green triangles correspond to the simulations performed with the detailed geometrical model implemented in BEAMnrc.

Both simulations followed closely the measured data across all four tube voltages. The differences were separately displayed at the lower panel of each subplot, showing the relative deviation between simulations and measurements. The largest difference for the CT particle source is 6.3 % and occurred for 80 kV at larger filter thicknesses. For the other voltages all deviations were smaller than 5 % and nearly all values the uncertainty ranges indicated by the error bars include zero. The BEAMnrc simulation showed over all smaller deviations with a maximum of 4.9 %.

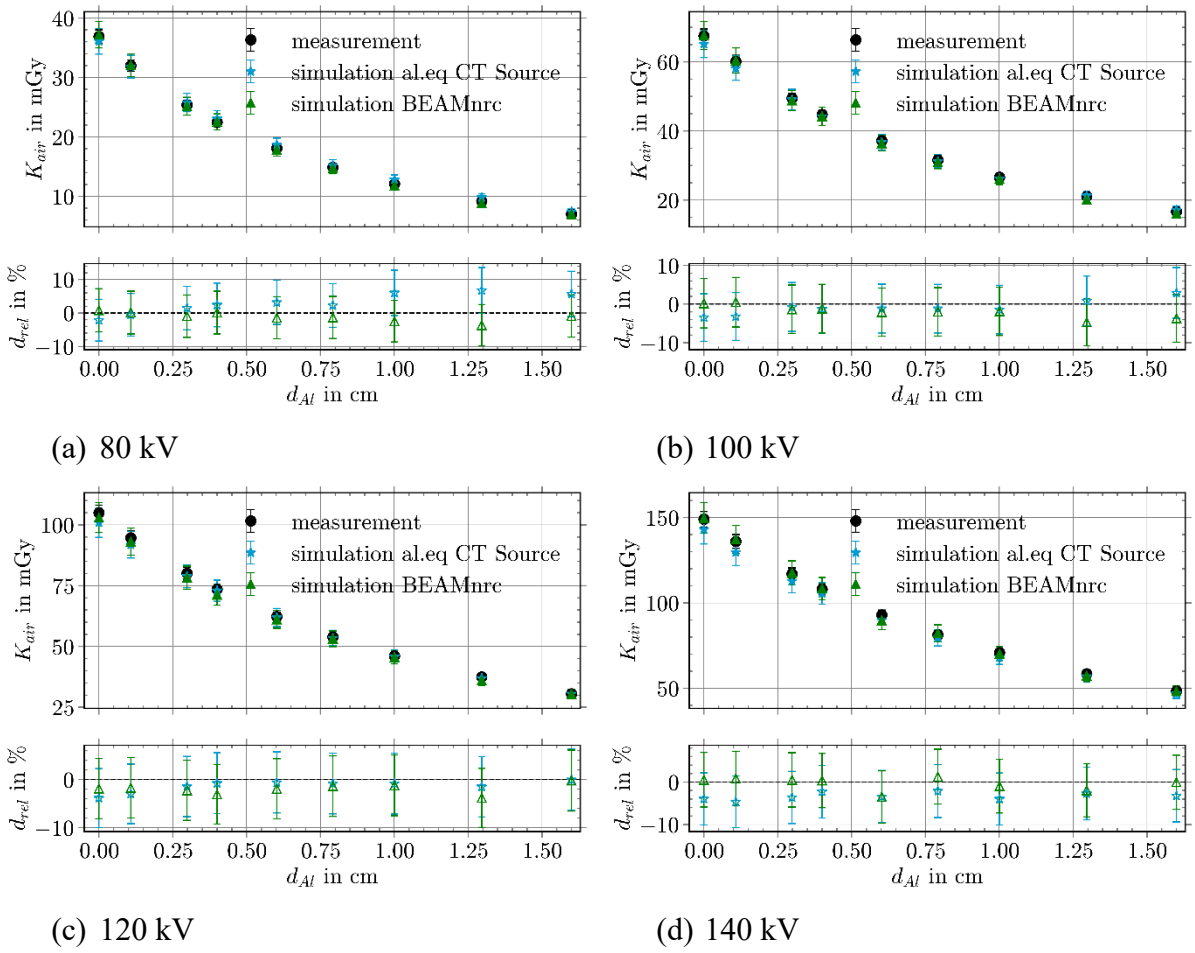

Figure 17. Comparison between measured and simulated aluminium attenuation curves for the four tube voltages. The top panels show air kerma values K_{air} in mGy as a function of the aluminium filter thickness d_{Al} (top), including measurement, a simulation using the evaluated source model and a reference simulation based on a detailed geometrical model. The bottom panels display the relative deviation of each simulation from the measured data.

Table 7. Comparison of aluminium HVL and mean energy between measured and simulated energy spectra.

		80 kV	100 kV	120 kV	140 kV
measurement	$E_{mean,exp}$ in keV	52.78	59.16	65.05	69.78
	HVL_{exp} in cm	0.623	0.720	0.834	0.911
al. eq. CT Source	$E_{mean,exp}$ in keV	53.05	59.21	64.94	69.56
	HVL_{exp} in cm	0.610	0.729	0.842	0.917
comparison	$E_{mean,exp}$/ $E_{mean,al.eq}$	0.999	0.999	1.002	1.003
	$HVL_{exp.}$/ $HVL_{al.eq}$	0.988	0.988	0.990	0.993

As an additional evaluation, **Table 7** shows the HVL (half value layer) and mean energy E_{mean} computed from the measured and simulated spectrum free in air. The experimentally determined spectrum was based on the aluminium attenuation curve as described in 2.4.1. The measured mean energies ranged from 52.78 keV at 80 kV to 69.78 keV at 140 kV, while HVL increased accordingly. The results for the CT particle source matched the experimental data within 0.3 % for the mean energies and 1.2 % for the HVLs.

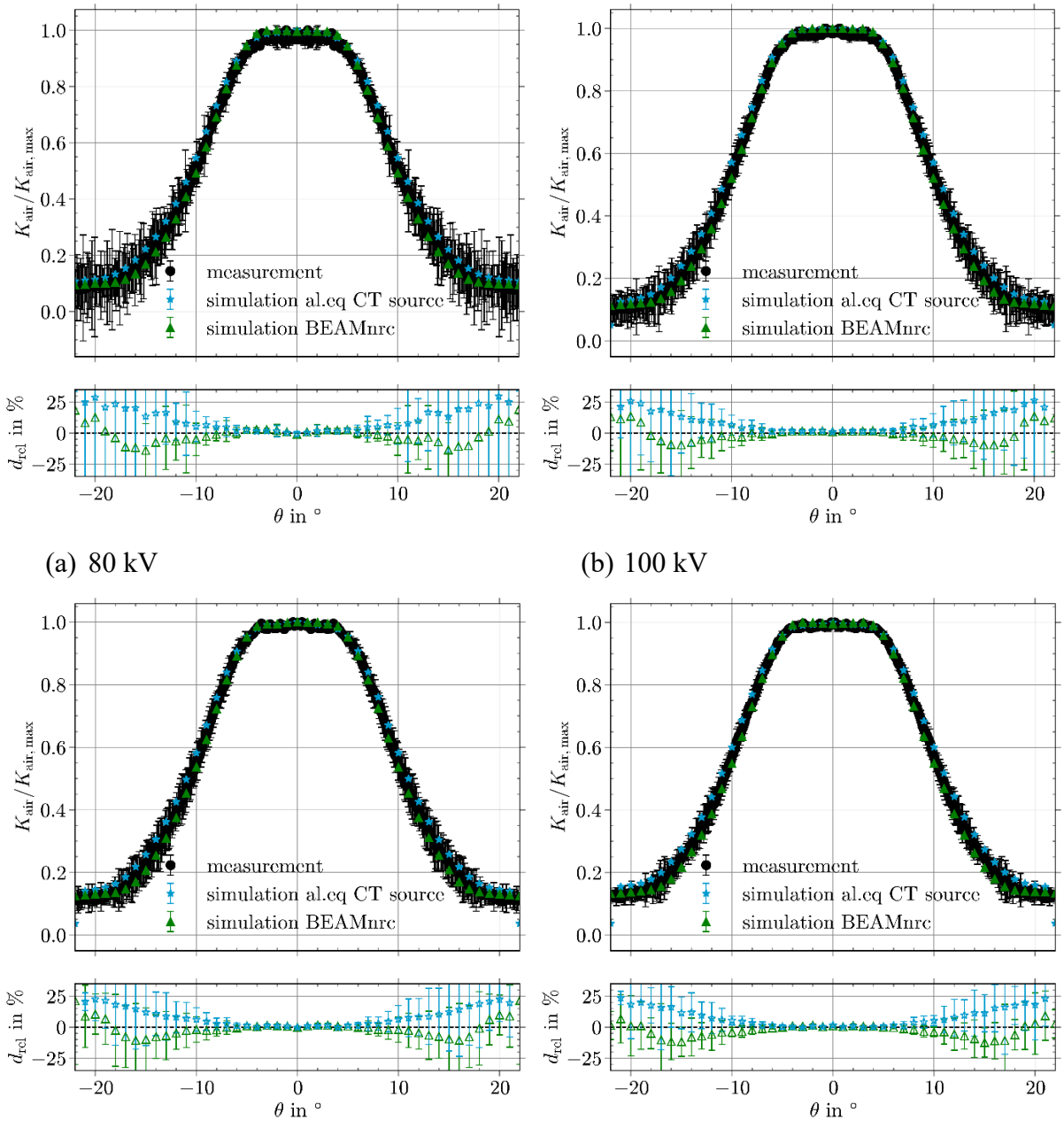

(a) 80 kV (b) 100 kV

(c) 120 kV (d) 140 kV

Figure 18. Comparison of bowtie filter attenuation profiles for the four tube voltages (top) and relative deviation between simulations and measurements (bottom).

For evaluation of the spatial distribution of the photon fluence the bowtie air kerma attenuation was measured and simulated. The comparison is shown in **Figure 18**. Both simulation approaches agreed with the measurements within the uncertainty range. The largest deviations were visible at the low dose edges of the distributions with deviations around 25 % for the aluminium equivalent CT source. In this area the measurement uncertainty was the largest. In the central area nearly, no deviation is visible.

3.1.2 Patient Table Density

To evaluate the phantom simulations, a correct representation of the patient table material was needed. The density was determined as described in 2.4.3.3. The graphical representation of the used method is shown in **Figure 19**. The determined fit parameter for the density dependent attenuation κ, the measured table attenuation and the calculated densities are presented in **Table 8**.

For the simulations an uncertainty weighted mean value $\rho_{\mathrm{mean}} = 2.15(28)\ g\ cm^{-3}$ of the four densities determined for the four tube voltages was used.

Table 8. Regression parameters, measured attenuation, resulting fitted density and corresponding regression parameters for each of the four CT tube voltages evaluated.

	a	b	ρ in g/cm^3	κ_{mess}
80 kV	-0.72457420(95)	0.9698542(54)	2.2061(31)	0.81
100 kV	-0.06982672(85)	0.9714593(48)	2.1691(29)	0.82
120 kV	-0.06779355(77)	0.9725538(43)	2.1027(27)	0.83
140 kV	-0.06688593(69)	0.9732707(39)	2.1420(26)	0.83

With the determined material density an angle resolved table air kerma attenuation profile was simulated and compared with the measured profile, presented in **Figure 20**. For the central area a mean deviation of 4.7 % was achieved. At the table edge the largest deviation of 53 % was seen.

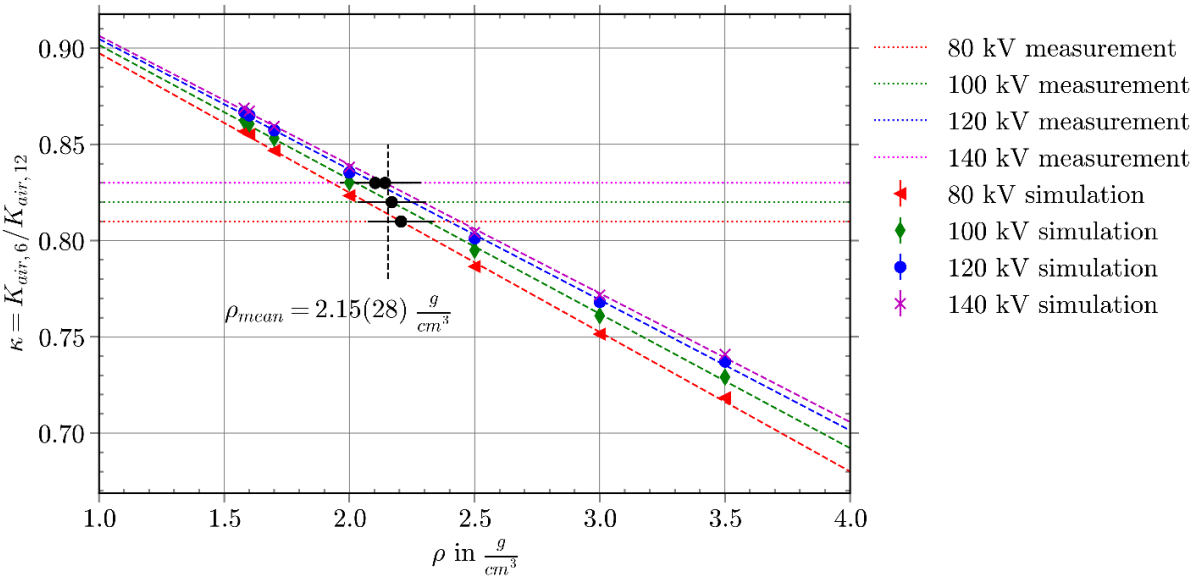

Figure 19. Patient table density dependent table attenuation for the four tube voltages and the linear fits. The dotted horizontal lines show the measurements results (same value for 140 kV and 120). The black dots represent the intersection points of the linear fit with measured values, from [1], Licensed under CC BY 4.0 (https://creativecommons.org/licenses/by/4.0/).

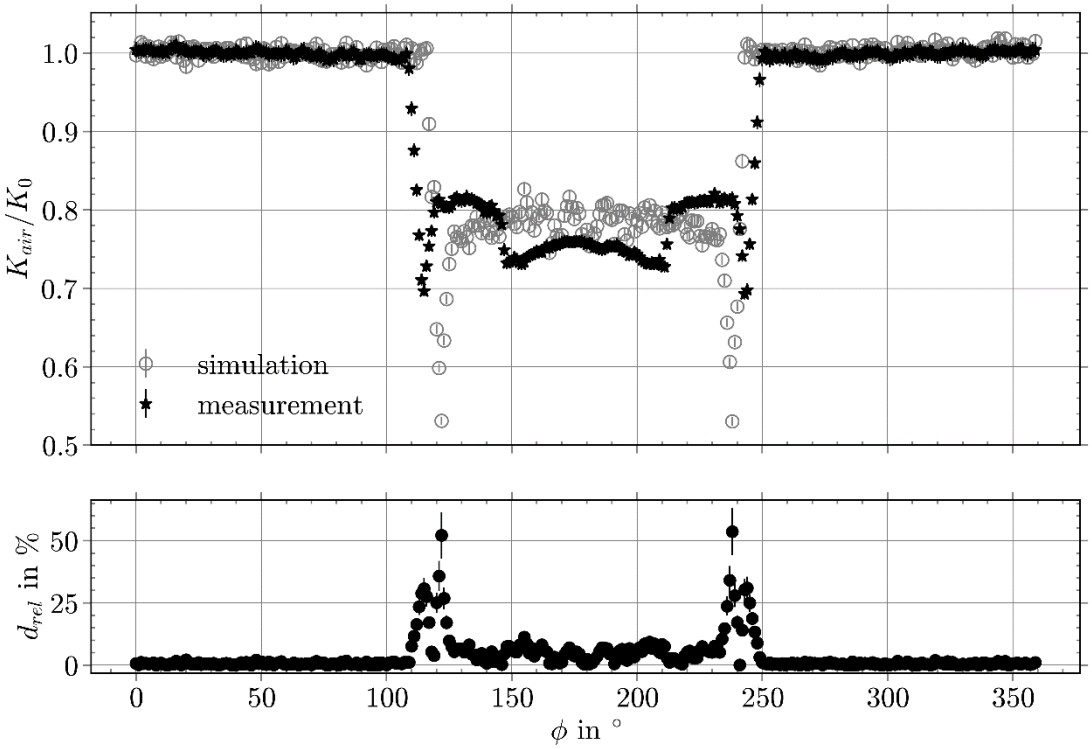

Figure 20. Comparison of the angular ϕ resolved air kerma attenuation profile of the patient table for a tube voltage of 140 kV. In the bottom panel the relative deviation between measurement and simulation is shown, from [1], Licensed under CC BY 4.0 (https://creativecommons.org/licenses/by/4.0/).

3.1.3 Phantom Validation

Table 9 and **Table 10** present the results for the comparison between measured and simulated air kerma values in the CTDI phantom and the anthropomorphic thorax phantom. The values were taken at five distinct positions within the phantoms: four peripheral positions (p12, p3, p6, p9) and one central position as depicted in **Figure 8**.

For the CTDI phantom the measured and simulated values showed agreement within the uncertainty range, shown as digits in the parentheses behind the values. The ratios between experimental and simulated values $K_{air,exp.}/ K_{air,sim}$ were close to one and deviations are mostly under 3 %. The largest deviations were visible in the phantom centre with a maximum of 5 % at 140 kV. For a tube voltage of 100 kV, the difference between measurement and simulations were less than 2 % for all positions.

Table 9. Comparison between measured and simulated air kerma values in a CTDI phantom for the GE Optima CT 660, from [1].

Voltage (kV)	Position	$K_{air,exp.}$ in mGy	$K_{air,sim.}$ in mGy	$K_{air,exp.}/ K_{air,sim.}$
80	p12	3.300(32)	3.28(18)	1.005(56)
	p3	3.210(31)	3.24(18)	0.992(55)
	p6	2.664(26)	2.67(15)	0.995(56)
	p9	3.217(32)	3.26(18)	0.987(55)
	centre	0.7411(73)	0.765(42)	0.969(54)
100	p12	6.280(62)	6.18(34)	1.017(57)
	p3	6.125(60)	6.08(33)	1.007(56)
	p6	5.161(51)	5.07(28)	1.018(57)
	p9	6.131(60)	6.12(34)	1.001(56)
	centre	1.636(16)	1.613(89)	1.017(57)
120	p12	9.988(98)	9.76(54)	1.023(57)
	p3	9.746(96)	9.61(53)	1.015(57)
	p6	8.293(81)	8.07(44)	1.028(57)
	p9	9.770(96)	9.67(53)	1.010(56)
	centre	2.836(28)	2.75(15)	1.032(58)
140	p12	14.37(14)	14.12(78)	1.020(57)
	p3	14.01(14)	13.89(76)	1.008(56)
	p6	12.02(12)	11.70(64)	1.025(57)
	p9	14.06(14)	13.97(77)	1.009(56)
	centre	4.312(42)	4.10(23)	1.050(59)

The comparison of air kerma values in the thorax phantom shown in **Table 10**, showed similar behaviour with slightly smaller deviations. The maximal deviation, also present in the central position of the phantom but at a tube voltage of 80 kV, was 4.8 %. At the peripheral position the discrepancies are within $\pm$2.6 %. For 100 kV all deviations were smaller than 2 %.

Table 10. Comparison between measured and simulated air kerma values in a thorax phantom for the GE Optima CT 660, from [1].

Voltage (kV)	Position	$K_{air,exp.}$ in mGy	$K_{air,sim.}$ in mGy	$K_{air,exp.}/ K_{air,sim.}$
80	p12	3.599(35)	3.67(20)	0.979(55)
	p3	3.019(30)	3.10(17)	0.974(54)
	p6	2.900(28)	2.90(16)	1.000(56)
	p9	3.025(30)	3.07(17)	0.984(55)
	centre	1.242(12)	1.304(72)	0.952(53)
100	p12	6.935(68)	6.97(38)	0.995(56)
	p3	5.796(57)	5.87(32)	0.988(55)
	p6	5.634(55)	5.54(30)	1.017(57)
	p9	5.818(57)	5.83(32)	0.997(56)
	centre	2.713(27)	2.73(15)	0.993(55)
120	p12	11.07(11)	11.01(61)	1.005(56)
	p3	9.406(92)	9.35(51)	1.006(56)
	p6	9.102(89)	8.86(49)	1.027(57)
	p9	9.320(91)	9.29(51)	1.004(56)
	centre	4.669(46)	4.65(26)	1.004(56)
140	p12	15.91(15)	15.90(87)	1.001(56)
	p3	13.46(13)	13.59(75)	0.990(55)
	p6	13.06(13)	12.88(71)	1.014(57)
	p9	13.49(13)	13.50(74)	0.999(56)
	centre	7.096(70)	6.94(38)	1.023(57)

In summary the simulation results closely match the experimental measurements across all tube voltages and positions. The observed deviations lied within the combined uncertainty of measurements and simulations.

3.1.4 Uncertainties

To calculate the uncertainties of the air kerma values determined with the simulations described the model equation presented as equation (28) was used. Each parameter in the equation has an uncertainty associated with it, denoted as σ_i and listed in **Table 11**. The combined uncertainty results in 5.5 % (k=1).

For the measurements using the RC0.6 Farmer-type chamber the uncertainty budget is presented in **Table 12**.

Table 11. Listed uncertainty budget for air kerma simulations with the implemented aluminium equivalent CT source using the MC framework EGSnrc, from [1].

Component	Symbol	Impact on simulation with EGSnrc $\mu_{\mathrm{A,B}}$ (%)
The shape of the bowtie filter (BT)	σ_{BT}	2.5
Spectrum	σ_{SPEC}	4.6
Air kerma Normalization	σ_{N}	0.7
Statistic Uncertainty	σ_{STAT}	0.1
Material Definition	σ_{M}	1.3
CT scanner's table density	$\sigma_{\rho_{\mathrm{T}}}$	0.04
Combined uncertainty (k = 1)	$\sigma_{\mathrm{c,sim}}$	5.5

There two different budgets for measurements in free air and in the phantoms. They differ mainly in the reproducibility uncertainty, which was in free air $\sigma_{\mathrm{R}} = 0.34\,\%$ and for measurements in phantoms $\sigma_{\mathrm{R}} = 0.75\,\%$. The values were determined by five times positioning and measuring in the respective setup. The resulting combined uncertainties were free in air $\sigma_{\mathrm{c,exp}} = 0.72\,\%$ $(k = 1)$ and for the phantom measurements $\sigma_{\mathrm{c,exp}} = 0.98\,\%$ $(k = 1)$.

Table 12. Uncertainty budget for air kerma measurements free in air and in phantoms, from [1].

Component	Symbol	Impact on air kerma free in air $\mu_{\mathrm{A,B}}$ (%)	Impact on air kerma in phantom $\mu_{\mathrm{A,B}}$ (%)
Measured Value for Charge	σ_Q	0.074	0.029
Calibration Coefficient	σ_{N_k}	0.48	0.48
Electrometer	σ_E	0.10	0.10
Spectral Smearing	σ_{k_Q}	0.38	0.38
Reproducibility	σ_{R}	0.34	0.75
Temperature	σ_T	0.10	0.10
Air Pressure	σ_p	0.10	0.10
Combined uncertainty (k = 1)	$\sigma_{\mathrm{c,exp}}$	0.72	0.98

3.2 Dataset Generation

This section presents the results related to the generation of the training dataset used for neural network development. It includes the evaluation of the anatomical volume distributions derived from the XCAT phantom dataset, ensuring the simulated anatomy is representative of the real patient data. Additionally, the radiation field input was validated by comparing the used algorithm to a full Monte Carlo simulation.

3.2.1 Virtual Phantoms

To evaluate the anatomical properties of the generated XCAT phantom dataset, a comparative analysis of the organ volume distributions against those from the real patient (RP) data was conducted. **Figure 21** presents histograms of organ volumes across 17 different anatomical structures, with XCAT data shown in blue and real patient data shown in orange.

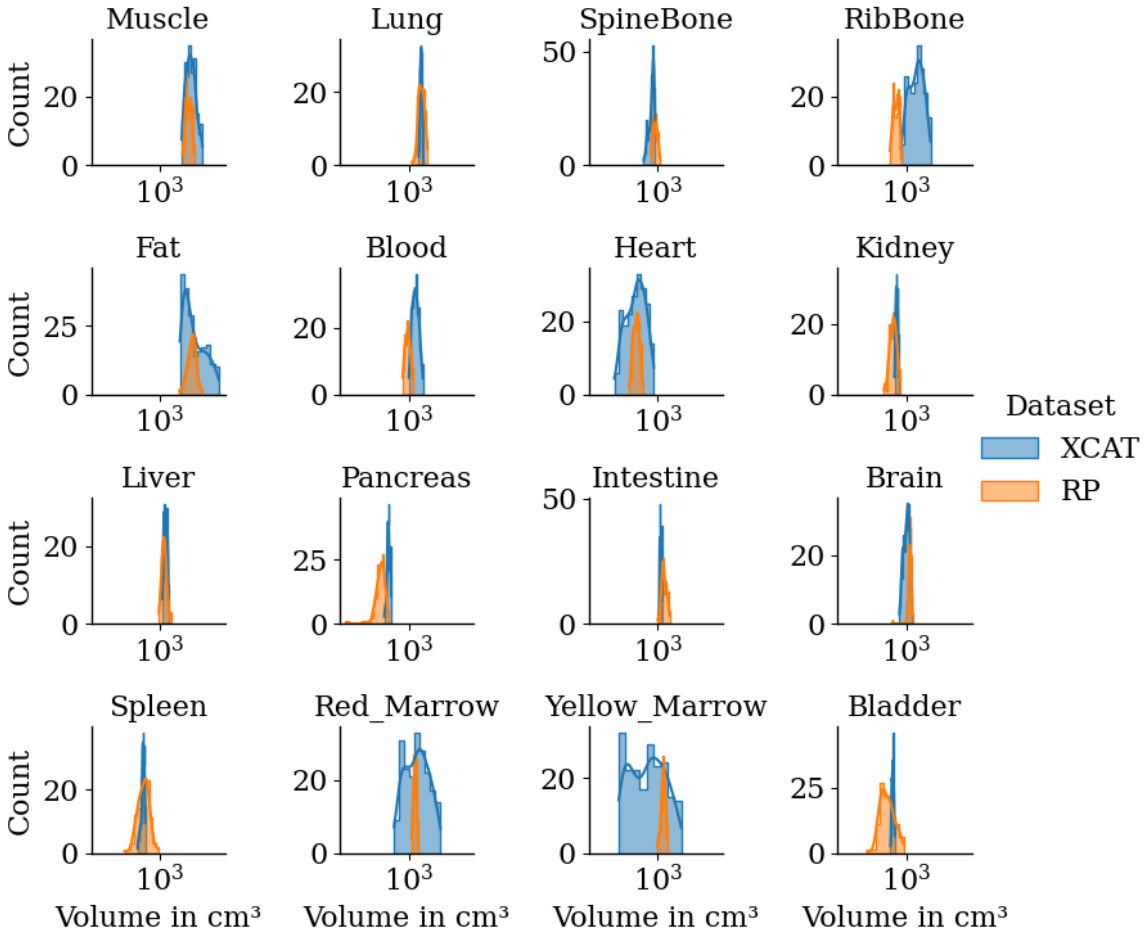

Figure 21. Comparison of organ volume distributions between XCAT dataset and real patient dataset for 17 organs.

Overall, the XCAT dataset replicates the main trends observed in patient anatomy, although some differences in distribution width and central tendency are apparent. The XCAT phantoms were deliberately designed to have a volume distribution that is broader than or comparable to the RP data to ensure sufficient anatomical variability for training robust neural network models.

Larger structures such as fat, muscle and liver show slightly broader distributions in XCAT, while the RP data tend to be more tightly clustered. For smaller organs, including heart, kidney and pancreas, the two datasets show similar mean volumes, although real patient data often show less variation between subjects.

There is good agreement for bony structures such as spine bone and rib bone, although XCAT volumes are often slightly larger, reflecting the intention to cover a wider range of body types. Organs with physiologically variable volumes, such as the bladder and spleen, show greater scatter in the real patient data - highlighting dynamics that are not fully modelled in the static XCAT representations.

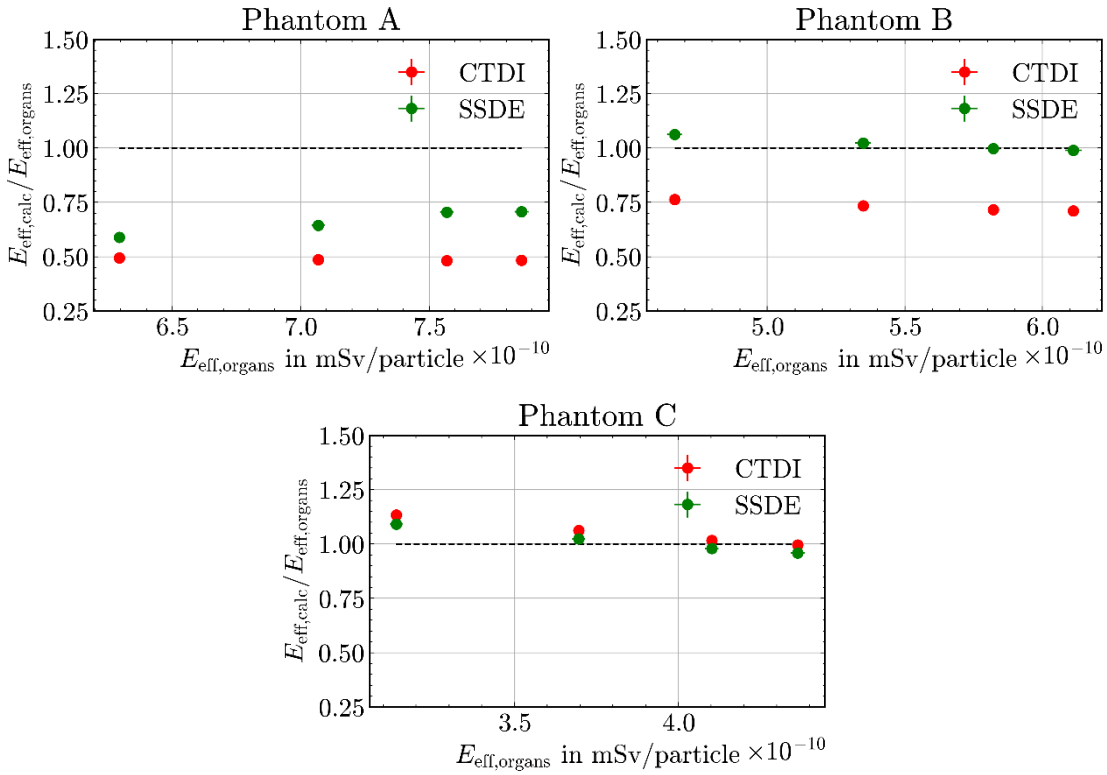

Figure 22. Comparison of effective dose estimates using CTDI and SSDE vs. organ-based effective dose estimate for 3 different sized XCAT phantoms, simulated for the four tube voltages 80 kV, 100 kV, 120 kV and 140 kV, from [2].

As a second evaluation we had a look at dosimetric quantities. The evaluation was presented in [2] and shown in **Figure 22**. The figure presents the ratio of CTDI and SSDE based calculated effective dose and organ dose based effective dose $E_{\text{eff,calc}}/E_{\text{eff,organ}}$ as a function of organ based effective dose $E_{\text{eff,organ}}$ simulated for the four different tube voltages 80 kV, 100 kV, 120 kV and 140 kV and three different phantoms.

For the small-sized phantom A, the effective dose derived from CTDI values underestimated the reference dose $E_{\text{eff,organ}}$ by approximately a factor of two. When SSDE was used in place of CTDI, the deviation was reduced but remained high as 30 %. In the case of phantom B, the effective dose calculated using CTDI showed a maximum deviation of 41 % from the reference. Substituting SSDE for CTDI markedly improved the agreement, with deviations reduced to within 6 %. For phantom C, both CTDI- and SSDE-based estimates slightly overestimated the effective dose, the largest discrepancies observed at the lowest tube voltage.

This behaviour reproduced the trend seen in literature [17].

3.2.2 Radiation Field Input

The radiation field input was calculated as described in section 2.5.2.3.

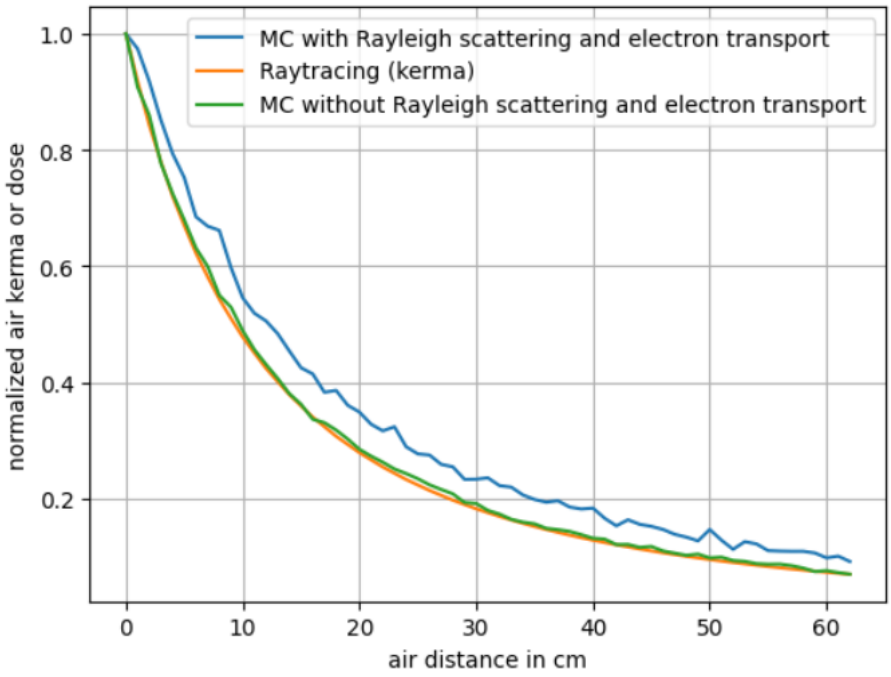

Figure 23. Comparison of normalised air kerma or dose as a function of distance in water, calculated using three methods for 120 kV spectrum: MC simulation with Rayleigh scattering and electron transport (blue), attenuation-based kerma calculation (orange) and MC simulation without Rayleigh scattering and electron transport (green).

Figure 23 presents the normalized air kerma attenuation or dose as a function of distance in water, comparing results from three methods: in blue a full Monte Carlo simulation including Rayleigh scattering and electron transport, in orange an attenuation calculation and a Monte Carlo simulation excluding Rayleigh scattering and electron transport in green. The attenuation-based air kerma calculation shows good agreement with the Monte Carlo simulation without Rayleigh scattering and electron transport, confirming the accurate reproduction of the primary photon attenuation in water.

The full Monte Carlo simulation, which includes Rayleigh scattering and electron transport, shows consistently higher values along the beam path. The increase reflects the contribution of scattered photons and secondary electrons that are not captured by the simplified approaches. Nonetheless, for the purpose of modelling primary beam attenuation, the raytracing method provides a sufficiently accurate and computationally efficient alternative to full Monte Carlo simulation.

3.3 Dose Calculation U-Net

3.3.1 Network Performance and Dataset Evaluation Without Uncertainties

Figure 24 showing violin plots of the distribution of relative deviations between NN-estimated and MC-simulated organ doses across all patients and organs. Each violin plot summarizes the spread of deviations for a specific training configuration. The 0 % NN shows a wide distribution with pronounced outliers, while the 10 % and 20 % NNs display narrower distributions centred closer to zero. The 100 % real-data model achieves the tightest distribution overall.

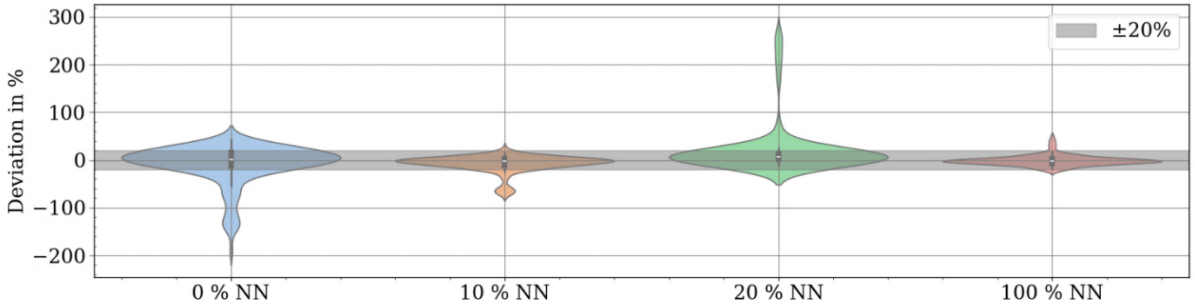

Figure 24. Relative deviation of organ dose estimations between MC simulation results for the 28 real patient test data cases.

Table 13 quantitatively summarizes the accuracy of summed organ dose predictions using three deviation thresholds. The performance of the networks in estimating summed organ doses was

evaluated by comparing their outputs to MC reference simulations. Performance metrics included pass rates at relative deviation thresholds (<7 %, <10 %, <20 %).

At 0 % NN, only 10 % and 30 % of predictions fall within 7 % and 10 % deviation thresholds, respectively, with a full pass rate only achieved at the <20 % deviation level. The mean deviation in this case is 11 %, the highest among all tested configurations.

In contrast, networks trained with 10 %, 20 % and 100 % real data all show a substantial improvement. For these configurations, pass rates at the <7 % and <10 % thresholds are markedly higher, ranging from 60–80 % and 90 % respectively. All three models reach 100 % pass rate at <20 % deviation, with a consistent mean deviation of 5 %.

Looking at the absolute deviation for an assumed tube current of 200 mA, the overall agreement of the organ doses were smaller than 0.5 mGy, with an increasing percentage when incorporating real patient data.

An organ-level analysis, presented in the appendix (**Table 15**), demonstrated that predictive accuracy varied considerably across different anatomical regions. Small-volume organs (e.g., gallbladder, esophagus) and organs located outside the primary irradiated field (e.g. stomach, colon, kidneys) exhibit higher relative deviations from MC dose estimates. These discrepancies are likely due to a combination of factors, including increased inter-patient anatomical variability, lower absolute dose levels and reduced signal-to-noise ratios in the MC ground truth for such regions. Larger deviations showed in most cases an overestimation by the NNs.

These results indicate that incorporating even a small percentage (10 %) of real patient data significantly improves the accuracy of NN-based dose predictions. Together, **Figure 24** and **Table 13** demonstrate that incorporating even a modest amount of real patient data during training significantly enhances both spatial and statistical accuracy of dose predictions.

Table 13. Percentage of pass rate of predicted organ doses for different accuracy levels for the four different networks. Top: Absolute deviation for an assumed current value of 200 mA, Bottom: Relative deviations for summed organ doses between MC and NN.

Deviation	**0 % NN**	**10 % NN**	**20 % NN**	**100 % NN**
< 0.1 mGy	52 %	69 %	62 %	72 %
< 0.2 mGy	68 %	81 %	84 %	84 %
< 0.5 mGy	88 %	96 %	94 %	95 %
< 7 %	10 %	60 %	60 %	50 %
< 10 %	30 %	90 %	90 %	90 %
< 20 %	100 %	100 %	100 %	100 %
Mean deviation	11 %	5 %	5 %	5 %

3.3.2 Network Performance and Dataset Evaluation With Uncertainties

The training of the uncertainty NNs resulted in slightly higher deviations from the MC ground truth data, as shown in **Table 14**. Additionally, this can be seen by looking at the organ dose deviations presented in **Table 15**. The models trained with real data still showed 100 % pass rate for deviations smaller than 20 % and a similar dependence on the incorporation of real patient data. The table also summarizes the aleatoric, epistemic and total uncertainty components of the different models. A clear dependence between the overall model uncertainty and the fraction of real data used during the training can be observed. The aleatoric uncertainty remains nearly constant at about 6 % for models trained predominantly on synthetic data, with a slight reduction to 3.6 % for the network based entirely on real cases. In contrast, the epistemic uncertainty decreases substantially from 6.2 % for the 0 % NN to 2.6 % for the 20 % NN, illustrating that even a limited amount of real data markedly improves model robustness and predictive confidence. The increase for the 100 % NN could be a sign of less variability of data compared to the mixed data sets.

Consequently, the total combined uncertainty shows a continuous decline from 17.8 % (k = 2) to 10 % (k = 2).

Table 14. Percentage of pass rate of estimated summed organ doses for different accuracy levels for the four different networks, presented as relative deviations for summed organ doses between MC and NN. In addition, the uncertainty components and the resulting extended combined uncertainty is shown, adapted from [4].

rel. deviation	Pass rate	$\sigma_{\text{aleatoric}}(x)$	$\sigma_{\text{epistemic}}(x)$	Combined uncertainty u_{tot}, k = 2
		0 % NN		
< 7%	3.6 %			
< 10%	3.6 %	6.1 %	6.2 %	17.8 %
< 20%	50.0 %			
mean deviation	**21 %**			
		10 % NN		
< 7%	86 %			
< 10%	89 %	6.2 %	3.9 %	14.6 %
< 20%	100 %			
mean deviation	**3.9 %**			
		20 % NN		
< 7%	86 %			
< 10%	93 %	6.3 %	2.6 %	13.6 %
< 20%	100 %			
mean deviation	**4.1 %**			
		100 % NN		
< 7%	75 %			
< 10%	86 %	3.6 %	3.5 %	10.0 %
< 20%	100 %			
mean deviation	**5.4 %**			

In **Figure 25** an example of the predicted dose maps, the deviations from the ground truth data and the predicted combined uncertainty (k = 1) were shown. Deviations from the MC reference are mainly observed outside the primary radiation fields. All networks reproduce the overall spatial dose pattern of the reference, but there are subtle differences between the models, especially in the peripheral regions. The model trained on synthetic data only (0 % NN) shows larger discrepancies in high dose areas within the bone, corresponding to regions of increased prediction uncertainty. Overall, the uncertainty maps closely reflect the spatial structure of the

deviation maps - areas of greater deviation from the ground truth generally coincide with regions of higher uncertainty, especially outside the main field.

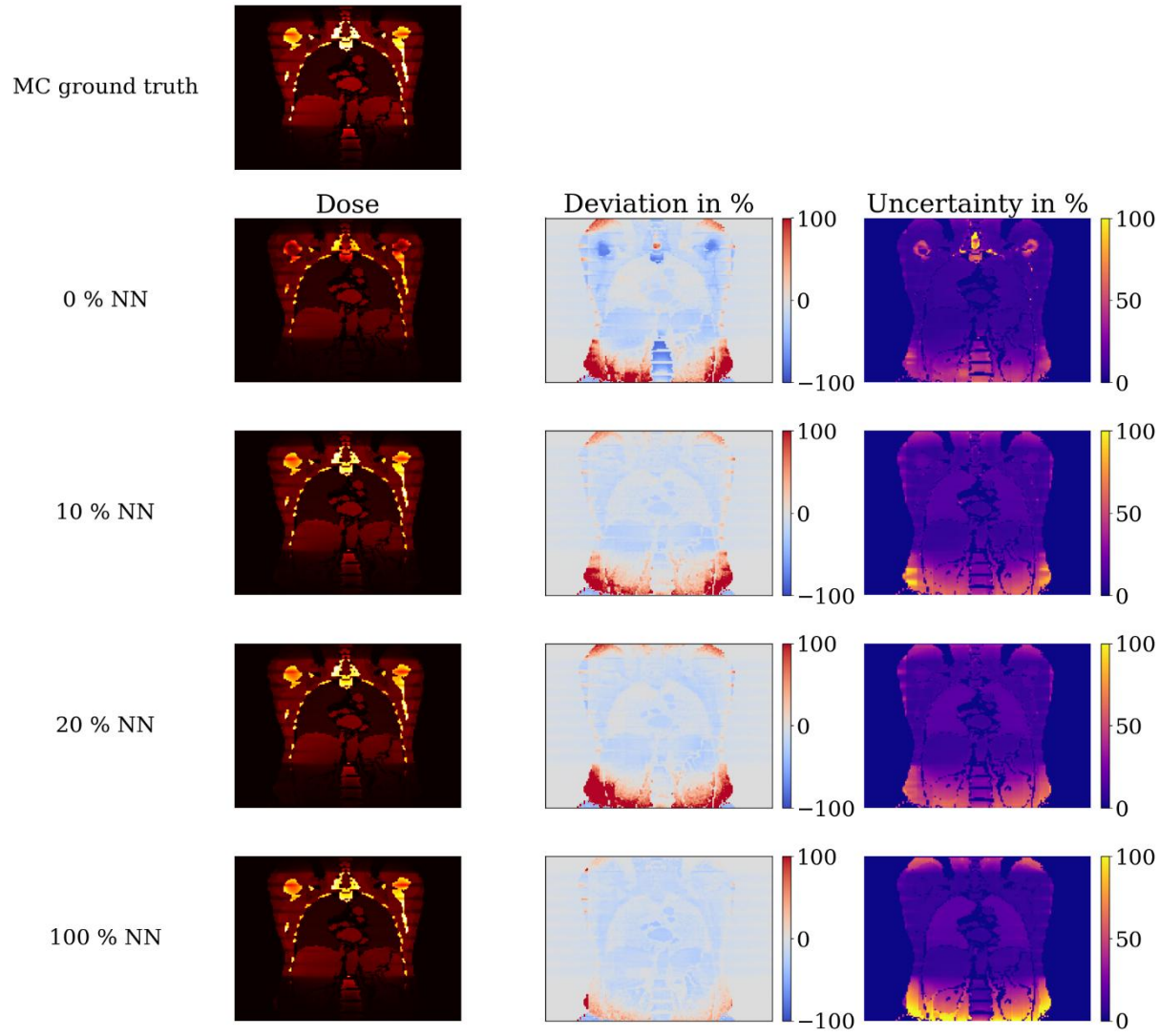

Figure 25. Example of a predicted dose map based on a real patient geometry (left). The corresponding relative deviations between NN und MC are shown in the middle. In the right column the uncertainty is shown, from [4].

4. Discussion and Outlook

The overall aim of this thesis was to establish a framework for personalised CT dosimetry using machine learning methods, explicitly addressing the evaluation of uncertainty at every stage of the process. By combining MC simulations, machine learning–based dose prediction and uncertainty propagation, the work presented here contributes to the process of developing clinically practical tools for patient- and organ-specific dose estimation. In contrast to traditional CT dose metrics such as CTDI and conversion factors, the approach developed in this study allows for individualized dose assessment that can be adapted to patient geometry and measured scanner parameter. Furthermore, the explicit inclusion of uncertainty evaluation provides a level of metrological robustness that is often lacking in current machine learning applications to medical imaging dosimetry.

4.1 Particle Source Implementation and Validation

A fundamental prerequisite for this framework was the development and validation of a reliable MC simulation environment capable of providing reference dose distributions for both training and validation of the machine learning models. For this purpose, a dedicated particle source class, tailored to the needs of CT dosimetry, was implemented within the EGSnrc MC framework. The validation of this source was performed in several systematic steps. In the first step, free-in-air simulations and measurements were compared in order to assess the accuracy of the simulated X-ray output. The simulated and measured aluminium attenuation curves showed excellent agreement, with all differences within the stated uncertainties. The largest deviation observed was about 6.9 % for the 80 kV spectrum, while the average deviation over all energies was only about 2.4 %. The bowtie filter characterisation also showed good agreement between measured and simulated profiles, with most data points agreeing within their respective uncertainty limits.

In the second validation stage, the simulated air kerma values were compared with experimental measurements in two different phantom setups including the absorption properties of the patient table. For air kerma measurements within the phantoms, simulations and measurements agreed to within about 5 %. Slightly larger deviations were found in the central regions of the phantoms, which showed an energy-dependent trend. With increasing tube voltage, the simulated air kerma values tended to underestimate the measurements in the central region. This discrepancy is probably related to the spectral composition of the simulated X-ray beam, which may have been slightly softer than in the experimental setup. The simplified bowtie filter model, implemented as varying aluminium thicknesses, does not fully reproduce the beam

hardening typically introduced by additional copper filtration as specified in IEC 61267:2005. Consequently, the resulting photon spectrum may have had a lower mean energy, leading to the observed underestimation of the central dose. The overall evaluated uncertainty of the MC simulation results was about 5.5 % (k = 1), which is a conservative estimate. Within this uncertainty range, all simulated values agreed with the experimental results, corresponding to a 68 % confidence interval. This comprehensive validation confirmed the reliability of the developed MC framework as a basis for generating high quality, traceable dose data for subsequent machine learning applications.

4.2 Dose Prediction Network Performance and Limitations

A major achievement of this work was the successful implementation of a neural network capable of predicting organ- and patient-specific dose values based on MC-generated training data, while also providing associated uncertainty estimates. The model's performance showed overall good agreement with reference MC results, meeting the IAEA TRS-457 guideline of a 20 % uncertainty limit for clinical dose estimation [71]. Although the predictions did not yet achieve the 7 % uncertainty level typically associated with experimental reference dosimetry [71]. The current results nevertheless indicate that the approach is a strong improvement over state-of-the-art clinical methods. The approach presented in this work achieves an accuracy comparable to other studies [27], [31], [32] reproducing MC results, while additionally introducing a systematic uncertainty approach.

An interesting finding was that the neural network trained without the uncertainty estimation layer achieved slightly better predictive accuracy than the version incorporating explicit uncertainty modelling. This observation suggests that while the inclusion of uncertainty modelling adds valuable interpretability and metrological information, it may also introduce additional training complexity. A potential strategy to overcome this limitation would be to employ a two-step training procedure in which a deterministic neural network is first optimized for accuracy and subsequently used as a starting point for the uncertainty-aware model. Such an approach could stabilize the learning process, reduce convergence issues and ensure that uncertainty propagation does not compromise predictive accuracy.

The uncertainty propagation framework implemented in this thesis assumes of Gaussian-distributed uncertainties, which allows for straightforward analytical propagation and interpretation. This simplification is justified by the statistical properties of the MC training data but may not fully capture asymmetric or multimodal uncertainty distributions arising from non-linear dependencies within the network. Despite this simplification, the comparison

between predicted uncertainties and empirical deviations from MC reference data showed good agreement, indicating that the Gaussian approximation provides a reasonable first order estimate for clinical applications. Nonetheless, future work could benefit from more sophisticated uncertainty quantification approaches like including adversarial attacks and comparing results to other uncertainty estimation methods like Bayesian neural networks.

For the data composition study, this work showed that organ dose estimation by neural networks is highly sensitive to the composition of the training data set. A model trained only on synthetic data performed poorly, with a total uncertainty of 17.8 % (k = 2), which is typical for an out-of-distribution behaviour [72]. Adding just 10 - 20 % real patient data greatly improved accuracy, reducing total uncertainties to below 15 %. Analysis of the uncertainty components showed that the aleatoric uncertainty remains almost constant, reflecting the inherent variability of the data, while the epistemic uncertainty decreases significantly - from 6.2 % to 2.6 % - when real data are introduced. This confirms that even small amounts of real patient data improve model confidence and generalisation. These findings are consistent with those of Khosravi et. al. [70], who reported optimal performance with 10% real data.

The current framework was trained and validated on a single scanner model and a limited range of scanning energies. Extending the approach to multiple scanner types and broader energy range will be essential for generalization and clinical transferability. Moreover, although synthetic data generation allowed for controlled and balanced sampling of parameter space, care must be taken to ensure that such synthetic data faithfully represent the variability observed in clinical practice. Experimental validation against direct dose measurements in anthropomorphic phantoms would provide an additional level of confidence in the model's performance and uncertainty estimates.

In addition, to look at the overall performance of the neural networks, we had a look at possible limitations, that must be addressed in future investigations.

Further analysis revealed residual dependencies in the model's predictions related to patient size as shown in **Figure 26**. All networks showed a similar relative size dependence. An examination of the absolute deviations revealed that the 10 % NN demonstrated the best performance. Although the networks were trained on a representative dataset including synthetic cases, the learned mapping between input quantities and dose still showed systematic variations with patient body dimensions. This indicates that geometric scaling effects were not fully captured by the current input feature set. The incorporation of size-dependent parameters, such as effective diameter, could help to minimize this dependence.

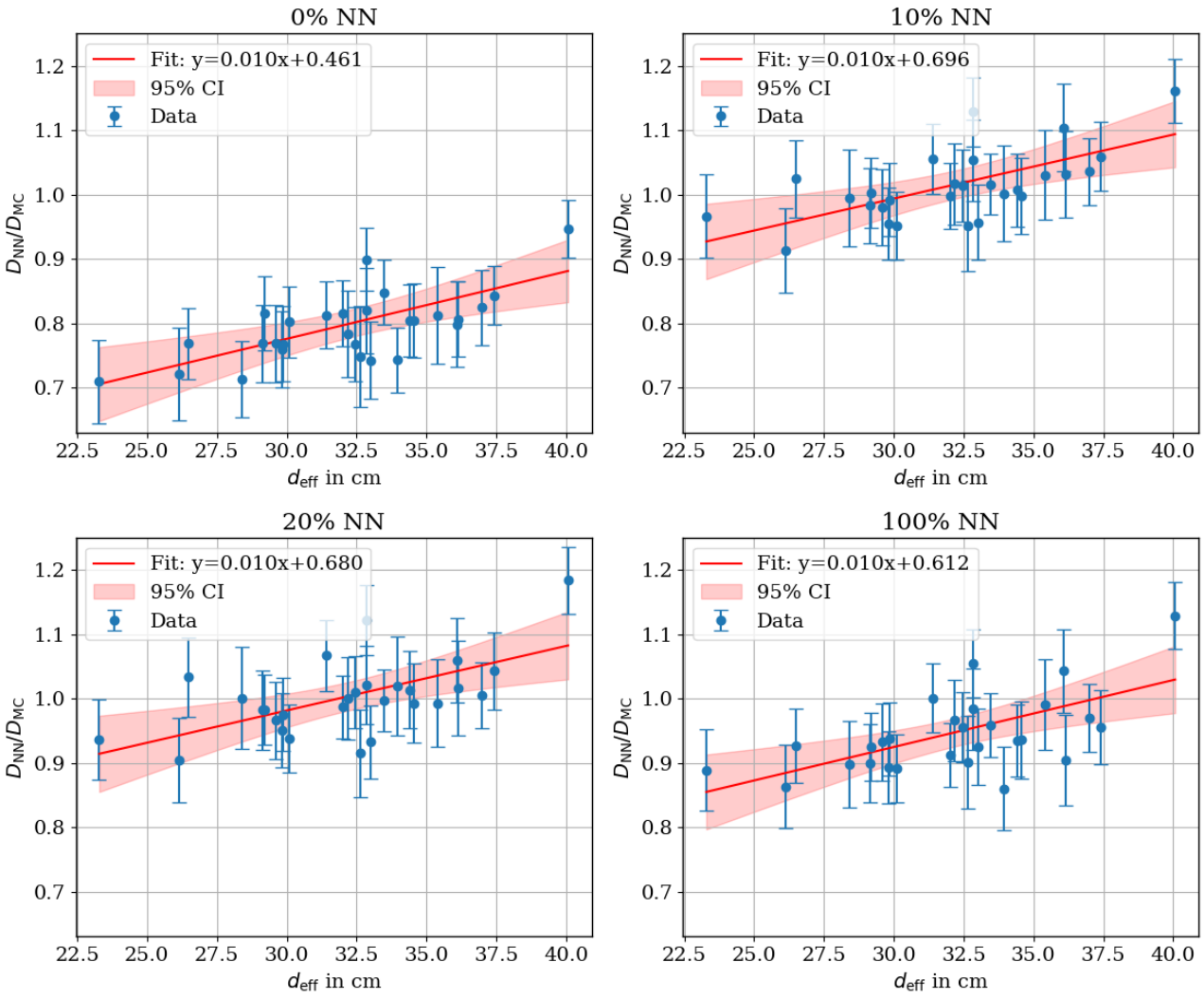

Figure 26. Ratio between NN estimated summed dose and MC based summed dose in dependency of the effective diameter of the patients, from [4].

Additionally, the network was found to be sensitive to patient translation within the field of view as presented by the PhD candidate in [3]. After training, the 0 % NN was also evaluated on a dedicated test dataset of synthetic data designed to simulate patient misalignment scenarios. For this purpose, laterally and vertically shifted versions of the original synthetic patient geometries were created and, the corresponding input electron density maps were shifted accordingly. This allowed a systematic assessment of the robustness of the network to patient positioning errors. **Figure 27** illustrates how the mean relative deviation of the estimated summed organ dose, compared to the reference MC results, changed as a function of positional displacement. For lateral displacements between 0 cm and 10 cm, the deviation increased progressively in the positive direction. At the reference (centred) position, the mean organ dose deviation was minimal (approximately -1.0 %) and served as a baseline. A lateral shift of 4 cm increased the mean deviation to approximately +3.3 %, which further increased to +9.2 % at

6 cm and +18.8 % at 8 cm. At the maximum evaluated displacement of 10 cm, a pronounced deviation of approximately -32.5 % was observed. The associated standard deviations, represented by the error bars in **Figure 27**, also increased with larger lateral displacements, reflecting the increasing sensitivity of the model to changes in patient geometry.

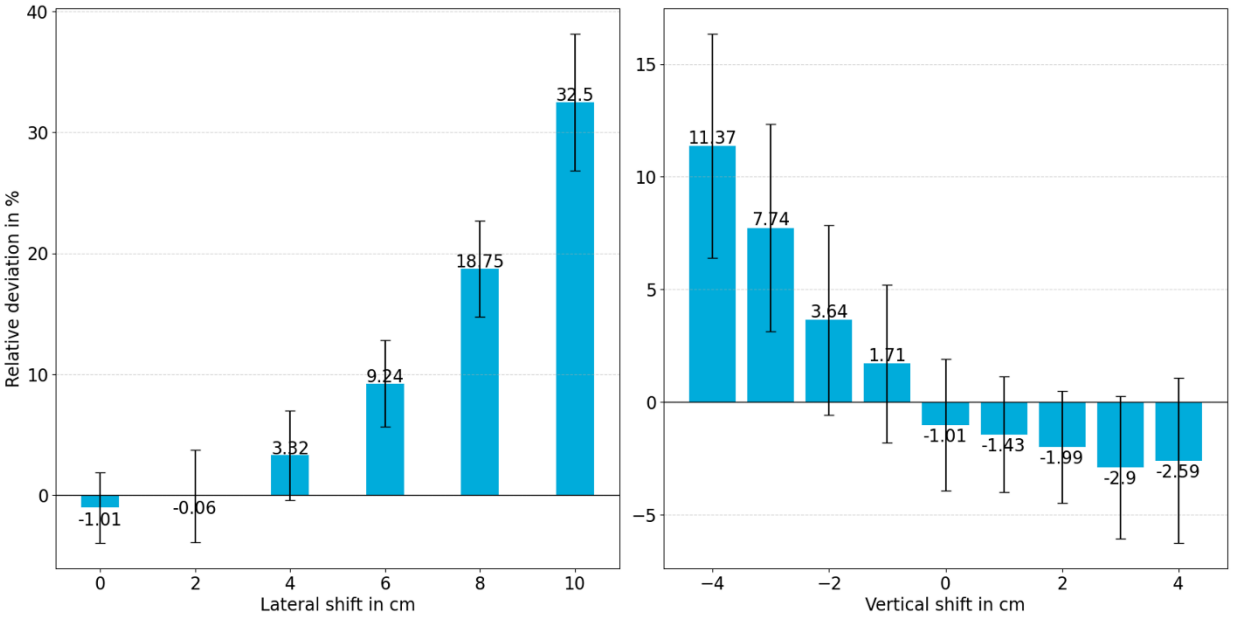

Figure 27. Mean relative deviation of summed organ doses between MC simulation and neural network estimation for different lateral (left) and vertical shifts (right). The error bars indicate the standard deviation of the XCAT test dataset, from [3].

In contrast, vertical displacements showed an asymmetric behaviour: downward (negative) displacements of the patient (-1 cm to -4 cm) resulted in increasingly positive deviations up to +11.4 %, while upward (positive) displacements resulted in increasingly negative deviations.

In **Figure 28** the relative deviation pattern between MC simulations and the neural network estimation for two lateral shift cases are further visualized, compared to the unshifted baseline for three example geometries from the test dataset. The results demonstrated that the current input encoding does not provide the network with explicit information about spatial positioning, leading to errors when patients were shifted relative to the scanner isocentre. To address this, future training datasets should include translated cases.

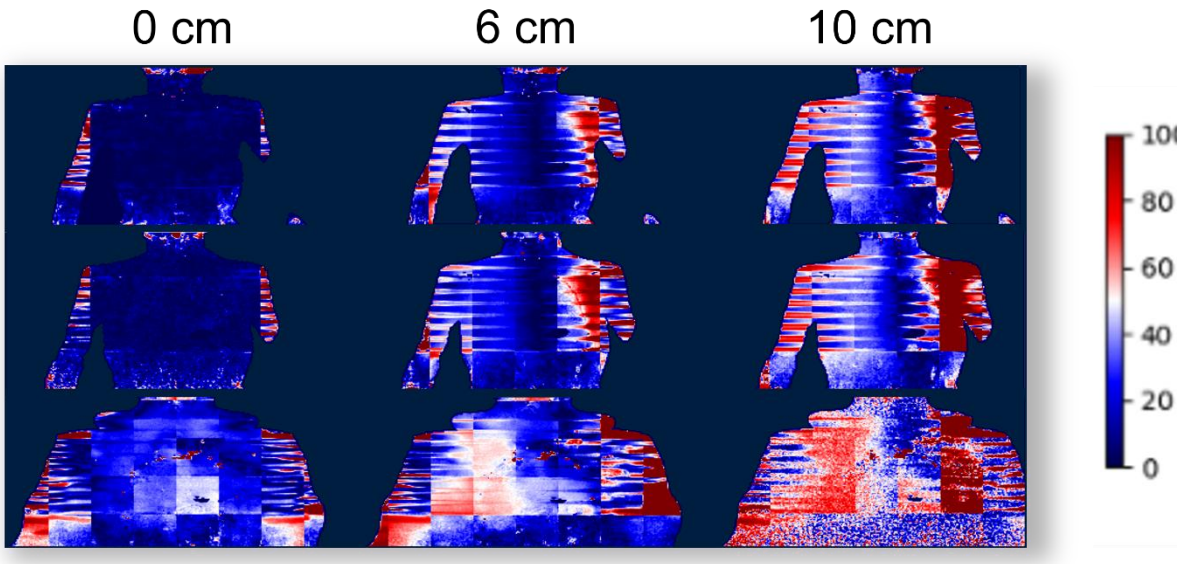

Figure 28. Relative deviation between MC simulation and neural network dose estimation for two different lateral shifts of the patient geometry compared to the unshifted case on the left for three different patient geometries from the test dataset.

5. Conclusion

This thesis presents the development and validation of a framework for personalised CT dosimetry based on machine learning, with explicit consideration of uncertainty at all stages of the process. By combining validated MC simulations, synthetic data generation and neural network-based dose estimations, the work demonstrated that machine learning can serve as a powerful and efficient tool for patient- and organ-specific dose estimation in clinical imaging to be able to generate a database of reliable dose values. Two main contributions were presented in this thesis.

First, a validated open-source particle source was developed, adaptable to real CT scanners using a simple set of measurements without the need of disclosed manufacturer information. A comprehensive uncertainty budget was also established to ensure reliable data generation.

Second, a neural network was implemented to predict organ doses with associated uncertainty estimates derived from the input data. The achieved prediction accuracy met the IAEA TRS-457 tolerance criteria of 20 % [71] uncertainty for clinical applications and significantly outperformed conventional CTDI or conversion factor-based methods. The explicit integration of uncertainty propagation into the machine learning framework represents an important methodological advance towards metrologically traceable, data-driven dosimetry.

In addition, the findings of this work suggest, that synthetic data, when supplemented with even a small amount of real patient data (10 %), can improve model development in personalised dosimetry. The wide, controllable anatomical diversity in synthetic data sets significantly improves model generalisation, while real data avoid the out-of-distribution problem.

Model evaluation revealed some dependence on patient diameter and positioning, indicating areas for improvement in input data design.

Overall, this work demonstrates that the integration of physics-based simulation with data-driven modelling offers a promising path towards accurate, uncertainty-aware and computationally efficient patient-specific dosimetry. The framework developed here lays the groundwork for extending machine learning-based dose prediction to different scanner types, energy spectra and clinical protocols. Future work should focus on refining the input parameterisation, improving the spatial generalisation and validating the predictions against experimental measurements in anthropomorphic phantoms.

In conclusion, this work represents a fundamental step towards the routine use of machine learning in clinical CT dosimetry.

6. Appendix

Table 15. Mean deviation in percent of organ doses between NN estimation and MC calculation

	0 % NN		**10 % NN**		**20 % NN**		**100 % NN**	
	Unc. NN	No Unc. NN	Unc. NN	No Unc. NN	Unc. NN	No Unc. NN	Unc. NN	No Unc. NN
Muscle	-11.1	7.0	-4.1	3.6	-4.6	8.2	-4.1	4.4
Lung	25.8	11.4	16.0	5.7	17.7	5.4	16.0	6.6
Fat	5.7	3.0	6.6	2.3	4.6	7.7	6.6	3.5
Blood	-1.3	9.6	5.6	10.8	1.3	6.4	5.6	6.6
Heart	-10.5	7.2	-1.7	6.4	-4.4	7.7	-1.7	6.1
Kidney	17.0	13.3	17.4	11.7	18.4	6.7	17.4	8.2
Liver	-3.1	9.4	0.7	7.9	0.8	7.9	0.7	6.4
Pancreas	-2.3	35.4	9.0	7.9	5.0	9.6	9.0	6.3
Brain	4.6	38.3	12.1	9.2	7.2	8.0	12.1	7.5
Spleen	-0.9	8.3	-0.7	6.3	-3.9	8.0	-0.7	6.4
Red Marrow	-37.4	26.5	-7.2	3.6	-8.0	4.1	-7.2	3.8
Stomach	844	13.0	755	7.8	800	9.8	755	7.7
Gallbladder	928	18.0	983	19.5	1074	27.1	983	27.3
Adrenal Gland	31.9	90.8	22.2	15.8	23.4	35.3	22.2	12.3
Colon	28.2	11.3	25.4	7.0	30	5.4	25.4	4.4
Oesophagus	2085	107.9	2089	64.2	2000	222.2	2089	10.0
Part. effective dose*	26.0	21.0	0.76	4.3	1.6	4.4	2.1	4.4

* Not all necessary organs for effective dose calculation were available in the segmentation software.

Table 16. Measurement results for density determination of PMMA probes from PTB measurement report 1.13-06.05.03/0004#0006 by working group 1.13.

Identifier	Density at $T = 20$ °C in g/cm^3	Uncertainty (k=2) in g/cm^3
Probe 1	1.1874	0.0010
Probe 2	1.1874	0.0010
Probe 3	1.1874	0.0010
Probe 4	1.1875	0.0010
Probe 5	1.1874	0.0010
Probe 6	1.1875	0.0010
Probe 7	1.1884	0.0010

References

[1] M.-L. Kuhlmann and S. Pojtinger, ‘Implementation of a new EGSnrc particle source class for computed tomography: validation and uncertainty quantification’, *PMB*, vol. 69, p. 095021, Apr. 2024, doi: 10.1088/1361-6560/ad3886.

[2] M.-L. Kuhlmann and S. Pojtinger, ‘Generation of a representative synthetic phantom dataset for the training of neural networks in personalized CT dosimetry’, in *Proceedings Virtual Imaging Trials in Medicine 2024*, Durham, NC: arXiv, May 2024. doi: 10.48550/ARXIV.2405.05359.

[3] M.-L. Kuhlmann and S. Pojtinger, ‘Impact of patient positioning on neural network organ dose estimation in CT’, in *Proceedings Virtual Imaging Trials in Medicine 2025*, Aug. 2025. doi: https://doi.org/10.5281/zenodo.16754124.

[4] M.-L. Kuhlmann, J. Martin, and S. Pojtinger, ‘Use of synthetic data for training dose prediction neural networks in CT dosimetry’, Jan. 2026, *arXiv*. doi: arXiv:2601.09235.

[5] R. A. Jucius and G. X. Kambic, ‘Radiation dosimetry in computed tomography (CT)’, *Proc. SPIE*, vol. 127, pp. 286–295, 1977.

[6] T. B. Shope, R. M. Gagne, and G. C. Johnson, ‘A method for describing the doses delivered by transmission x-ray computed tomography’, *Med. Phys.*, vol. 8, no. 4, pp. 488–495, July 1981, doi: https://doi.org/10.1118/1.594995.

[7] W. Kalender, W. Seissler, E. Klotz, and P. Vock, ‘Spiral volumetric CT with single-breath-hold technique, continuous transport, and continuous scanner rotation’, *Radiol. Soc. N. Am. RSNA*, vol. 176, pp. 181–183, July 1990, doi: https://doi.org/10.1148/radiology.176.1.2353088.

[8] Bundesamt für Strahlenschutz, ‘Umweltradioaktivität und Strahlenbelastung Jahresbericht 2020’, *Bundesminist. Für Umw. Naturschutz Nukl. Sicherh. Verbraucherschutz*, Oct. 2021, doi: urn:nbn:de:02212023092039261.

[9] D. J. Brenner, C. H. McCollough, and C. G. Orton, ‘It is time to retire the computed tomography dose index (CTDI) for CT quality assurance and dose optimization’, *Wiley*, vol. 33, no. 5, pp. 1189–1191, Apr. 2006, doi: 10.1118/1.2173933.

[10] NCRP, ‘Commentary No. 27 – Implications of Recent Epidemiologic Studies for the Linear-Nonthreshold Model and Radiation Protection’, National Council on Radiation Protection and Measurements, 27, 2018. [Online]. Available: https://ncrponline.org/shop/commentaries/commentary-no-27-implications-of-recent-epidemiologic-studies-for-the-linear-nonthreshold-model-and-radiation-protection-2018/

[11] M. Zankl, E. Panzer, and G. Drexler, ‘The calculation of dose from external photon exposures using reference human phantoms and Monte Carlo methods. Part VI: Organ doses from tomographic examinationsThe calculations of dose from external photon exposures using reference and realistic human phantoms and Monte Carlo methods’, *GSF-Rep. 3091*, 1991.

[12] P. C. Shrimpton, D. G. Jones, M. C. Hillier, B. F. Wall, J. C. Le Heron, and K. Faulkner, ‘Survey of CT practice in the UK. Part 2, Dosimetric aspects’, *NRPB-249*, 1991.

[13] European Comission, *European guidelines on quality criteria for computed tomography*, Report, 1999.

[14] ICRP, ‘The 2007 Recommendations of the International Commission on Radiological Protection’, International Commission on Radiological Protection, 103, 2007. [Online]. Available: https://www.icrp.org/publication.asp?id=ICRP+Publication+103

[15] J. M. Boone *et al.*, ‘Size-specific dose estimates (SSDE) in Pediatric and Adult Body CT Examinations’, *AAPM Rep. No 204*, 2011.

[16] ICRP, ‘Use of Dose Quantities in Radiological Protection’, International Commission on Radiological Protection, Publication 147, 2021. [Online]. Available: https://www.icrp.org/publication.asp?id=ICRP%20Publication%20147

[17] C. H. McCollough, S. Leng, L. Yu, D. D. Cody, J. M. Boone, and M. F. McNitt-Gray, ‘CT Dose Index and Patient Dose: They Are Not the Same Thing’, *Radiol. Soc. N. Am. RSNA*, vol. 259, no. 2, pp. 311–316, May 2011, doi: 10.1148/radiol.11101800.

[18] S. Ketelhut, M.-L. Kuhlmann, L. Büermann, L. Pirl, and M. Borowski, ‘Simulation study on the conversion between CT and CBCT dose quantities via the effective dose’, *IOP Publ.*, vol. 9, p. 065030, 2023, doi: https://doi.org/10.1088/2057-1976/ad065e.

[19] R. L. Dixon, ‘A new look at CT dose measurement: beyond CTDI’, *Wiley*, vol. 30, no. 6, pp. 1272–1280, May 2003, doi: 10.1118/1.1576952.

[20] K. Perisinakis, J. Damilakis, A. Tzedakis, A. Papadakis, N. Theocharopoulos, and N. Gourtsoyiannis, 'Determination of the weighted CT dose index in modern multi-detector CT scanners', *IOP Publ.*, vol. 52, no. 21, pp. 6485–6495, Oct. 2007, doi: 10.1088/0031-9155/52/21/010.
[21] V. J. Weier and J. Zhang, 'Technical Note: Using linear and polynomial approximations to correct IEC CTDI measurements for a wide-beam CT scanner', *Wiley*, vol. 46, no. 11, pp. 5360–5365, Sept. 2019, doi: 10.1002/mp.13799.
[22] L. Chroonsik, K. Kwang Pyo, W. E. Bolch, B. E. Moroz, and L. Folio, 'NCICT: a computational solution to estimate organ doses for pediatric and adult patients undergoing CT scans', *IOP Publ.*, vol. 35, no. 4, pp. 891–909, Nov. 2015, doi: 10.1088/0952-4746/35/4/891.
[23] J. Damilakis, 'CT Dosimetry What Has Been Achieved and What Remains to Be Done', *Ovid Technol. Wolters Kluwer Health*, vol. 56, no. 1, pp. 62–68, Jan. 2021, doi: 10.1097/RLI.0000000000000727.
[24] R. Schmidt, J. Wulff, and K. Zink, 'GMctdospp: Description and validation of a CT dose calculation system', *Am. Assoc. Phys. Med.*, vol. 42, no. 7, pp. 4260–4270, 2015, doi: 10.1118/1.4922391.
[25] E. Somasundaram, N. S. Artz, and S. L. Brady, 'Development and validation of an open source Monte Carlo dosimetry model for wide-beam CT scanners using Fluka', *J. Appl. Clin. Med. Phys.*, vol. 20, no. 4, pp. 132–147, Feb. 2019, doi: 10.1002/acm2.12559.
[26] M. Cros, R. M. S. Joemai, J. Geleijns, D. Molina, and M. Salvadó, 'SimDoseCT: dose reporting software based on Monte Carlo simulation for a 320 detector-row cone-beam CT scanner and ICRP computational adult phantoms', *Phys. Med. Biol.*, vol. 62, pp. 6304–6321, July 2017, doi: 10.1088/1361-6560/aa77ea.
[27] J. Maier, L. Klein, E. Eulig, S. Sawall, and M. Kachelrieß, 'Real-time estimation of patient-specific dose distributions for medical CT using the deep dose estimation', *Med. Phys.*, vol. 49, no. 4, pp. 2259–2269, Feb. 2022, doi: 10.1002/mp.15488.
[28] Z. Peng *et al.*, 'A method of rapid quantification of patient-specific organ doses for CT using deep-learning-based multi-organ segmentation and GPU-accelerated Monte Carlo dose computing', *Am. Assoc. Phys. Med.*, vol. 47, no. 6, pp. 2526–2536, June 2020, doi: 10.1002/mp.14131.
[29] M. Myrinakis, J. Stratakis, and J. Damilakis, 'Rapid estimation of patient-specific organ doses using a deep learning network', *Med Phys*, vol. 50, no. 11, pp. 7236–7244, Nov. 2023, doi: 10.1002/mp.16356.
[30] J. Damilakis, 'Artificial intelligence-powered personalized patient dosimetry in CT', *Oxf. Univ. Press OUP*, vol. 2, no. 1, Jan. 2025, doi: 10.1093/bjrai/ubaf007.
[31] Y. Salimi, A. Akhavanallaf, Z. Mansouri, I. Shiri, and H. Zaidi, 'Real-time, acquisition parameter-free voxel-wise patient-specific Monte Carlo dose reconstruction in whole-body CT scanning using deep neural networks', *Springer Sci. Bus. Media LLC*, vol. 33, pp. 9411–9424, June 2023, doi: 10.1007/s00330-023-09839-y.
[32] E. Tzanis and J. Damilakis, 'A machine learning-based pipeline for multi-organ/tissue patient-specific radiation dosimetry in CT', *Eur Radiol*, vol. 35, no. 2, pp. 919–928, Aug. 2024, doi: 10.1007/s00330-024-11002-0.
[33] M. Frid-Adar, I. Diamant, E. Klang, M. Amitai, J. Goldberger, and H. Greenspan, 'GAN-based synthetic medical image augmentation for increased CNN performance in liver lesion classification', *Elsevier BV*, vol. 321, pp. 321–331, Dec. 2018, doi: 10.1016/j.neucom.2018.09.013.
[34] Y. Salimi, I. Shiri, Z. Mansouri, and H. Zaidi, 'Development and validation of fully automated robust deep learning models for multi-organ segmentation from whole-body CT images', *Phys. Med.*, vol. 130, p. 104911, Feb. 2025, doi: 10.1016/j.ejmp.2025.104911.
[35] International comission on radiation units and measurements, 'Fundamental Quantities and Units for Ionizing Radiation', ICRU Report 60, Dec. 1998.
[36] The international comission on radation units and measurements, 'KEY DATA FOR IONIZING-RADIATION DOSIMETRY: MEASUREMENT STANDARDS AND APPLICATIONS', ICRU Report 90, Oct. 2016.

[37] The international comission on radation units and measurements, ‘RADIATION DOSE AND IMAGE-QUALITY ASSESSMENT IN COMPUTED TOMOGRAPHY’, ICRU Report 87, 2012.
[38] J. Bernoulli, *Ars conjectandi: Usum & Applicationem Praecedentis Doctrinae in Civilibus*. Basel: Thurnisiorum, 1713.
[39] I. Kawrakow, D. Rogers, E. Mainegra-Hing, F. Tessier, R. Townson, and B. Walters, *EGSnrc toolkit for Monte Carlo simulation of ionizing radiation transport*. (2000). C++, Fortran. National Research Council of Canada. [Online]. Available: https://nrc-cnrc.github.io/EGSnrc/
[40] P. Mayles, A. Nahum, and J. C. Rosenwald, *Handbook of radiotherapy physics - Theory and Practice*. Taylor & Francis Ltd, 2007.
[41] R. C. Larso and A. R. Odoni, *Urban Operations Research*, 2nd edn. New Jersey: Prentice Hall, 1981.
[42] A. J. Walker, ‘New fast method for generating discrete random numbers with arbitrary frequency distributions’, *Inst. Eng. Technol. IET*, vol. 10, no. 8, pp. 127–128, Apr. 1974, doi: 10.1049/el:19740097.
[43] M. J. Berger *et al.*, ‘XCOM-Photon Cross Sections Database, NIST Standard Reference Database 8 (XGAM) NIST, PML, Radiation Physics Devision’. Nov. 2010. doi: 10.18434/T48G6X.
[44] M. J. Berger, ‘Monte Carlo Calculation of the penetration and diffusion of fast charged particles.’, in *Methods in Comput. Phys.*, vol. 1, New York: Academic, 1963, pp. 135–215.
[45] I. Kawrakow, E. Mainegra-Hing, D. Rogers, F. Tessier, and B. Walters, ‘The EGSnrc Code System: Monte Carlo Simulation of Electron and Photon Transport’, NRC, Ottawa, Canada, NRCC Report PIRS-701, 2025.
[46] B. Alikhani and L. Büermann, ‘Non-invasive experimental determination of a CT source model’, *Phys. Med.*, vol. 32, no. 1, pp. 59–66, Jan. 2016, doi: https://doi.org/10.1016/j.ejmp.2015.09.006.
[47] S. Rosendahl *et al.*, ‘CT beam dosimetric characterization procedure for personalized dosimetry’, *Phys. Med. Biol.*, vol. 64, no. 7, p. 075009, Mar. 2019, doi: ht%20t%20p%20s%20:%20//d%20oi%20.or%20g%20/10%20.10%208%208/13%2061-%2065%206%200/a%20b%200%20e%209%207.
[48] B. Schmidt and W. Kalender, ‘A fast voxel-based Monte Carlo method for scanner- and patient-specific dose calculations in computed tomography’, *Phys. Med.*, vol. 18, no. 2, pp. 43–53, Apr. 2002.
[49] G. Poludniowski, A. Omar, R. Bujila, and P. Andreo, ‘Technical Note: SpekPy v2.0—a software toolkit for modeling x-ray tube spectra’, *Med. Phys.*, vol. 48, no. 7, pp. 3630–3637, July 2021, doi: https://doi.org/10.1002/mp.14945.
[50] J. M. Boone, ‘Method for evaluating bow tie filter angle-dependent attenuation in CT: Theory and simulation results’, *Med. Phys.*, vol. 37, no. 1, pp. 40–48, 2010, doi: https://doi.org/10.1118/1.3264616.
[51] W. H. Press, S. A. Teukolsky, W. T. Vetterling, and B. P. Flannery, *Numerical Recipes - The Art of Scientific Computimg*, 3rd edn. Cambridge, United Kingdom: Cambridge University Press, 2007.
[52] R. P. Brent, *Algorithms for Minimization without Derivatives*. New Jersey: Prentice-Hall, Englewood Cliffs, 1973.
[53] D. Rogers, B. Walters, and I. Kawrakow, ‘BEAMnrc Users Manual’, *NRCC Rep. PIRS-0509ArevL*, Feb. 2023.
[54] E. Mainegra-Hing, D. Rogers, R. Townson, B. Walters, F. Tessier, and I. Kawrakow, ‘The EGSnrc g application’, NRC, PIRS 3100, 2025. [Online]. Available: https://nrc-cnrc.github.io/EGSnrc/doc/pirs3100/
[55] D.W.O. Rogers, B. Walters, and I. Kawrakow, ‘BEAMnrc Users Manual’, NRC, NRCC Report PIRS-509, 2009.
[56] D. Grund, M. Orlishausen, and I. Taha, ‘Determination of fiber volume fraction of carbon fiber-reinforced polymer using thermogravimetric methods’, *Polym. Test.*, vol. 75, pp. 358–366, May 2019, doi: 10.1016/j.polymertesting.2019.02.031.
[57] W. Kaiser, *Kunststoffchemie für Ingenieure : Von der Synthese bis zur Anwendung Auflage*, 2nd edn. München: Carl Hansberg Verlag GmbH & Co. KG, 2007.

[58] BIPM *et al.*, *Evaluation of measurement data — Guide to the expression of uncertainty in measurement. Joint Committee for Guides in Metrology, JCGM 100:2008*, 2008. [Online]. Available: https://www.bipm.org/documents/20126/2071204/ JCGM_100_2008_E.pdf/cb0ef43f-baa5-11cf-3f85-4dcd86f77bd6.
[59] I. Goodfellow, Y. Bengio, and A. Courville, *Deep Learning*. Cambride, MA: MIT Press, 2016.
[60] O. Ronnenberger, P. Fischer, and T. Brox, 'U-Net: Convolutional Networks for Biomedical Image Segmentation', *Springer Int. Publ. Switz.*, vol. 9351, 2015, doi: https://doi.org/10.1007/978-3-319-24574-4_28.
[61] W. P. Segars, G. M. Sturgeon, S. Mendonca, J. Grimes, and B. M. W. Tsui, '4D XCAT phantom for multimodality imaging research.', *Med. Phys.*, vol. 37, no. 9, pp. 4902–4915, 2010, doi: 10.1118/1.3480985.
[62] C. H. Kim *et al.*, 'Adult Mesh-type Reference Computational Phantoms', *ICRP Publ. 145*, vol. 49, no. 3, 2020, [Online]. Available: https://www.icrp.org/page.asp?id=575
[63] A. Schegerer, R. Loose, L. Heuser, and G. Brix, 'Diagnostic Reference Levels for Diagnostic and Interventional X-Ray Procedures in Germany: Update and Handling', *Fortschr Röntgenstr.*, vol. 191, no. 08, pp. 739–751, 2019, doi: https://doi.org/10.1055/a-0824-7603.
[64] J. Wassethal *et al.*, 'TotalSegmentator: Robust Segmentation of 104 Anatomic Structures in CT Images', *Radiol. Soc. N. Am. RSNA*, vol. 5, no. 5, Sept. 2023, doi: 10.1148/ryai.230024.
[65] 'Photon, Electron, Proton and Neutron Interaction Data for Body Tissues', International Commission on Radiation Units and Measurements, ICRU Report 46, 1992.
[66] F. Lehner, P. Lombardo, S. Castillo, O. Hupe, and M. Magnor, 'RadField3D: a data generator and data format for deep learning in radiation-protection dosimetry for medical applications', *J. Radiol. Prot.*, vol. 45, no. 2, p. 021508, May 2025, doi: 10.1088/1361-6498/add53d.
[67] Lakshminarayanan, Balaji, Pritzel, Alexander, and Blundell, Charles, 'Simple and Scalable Predictive Uncertainty Estimation using Deep Ensembles', presented at the 31st Conference on Neural Information Processing Systems, Long Beach, CA, USA: arXiv, 2017. doi: 10.48550/ARXIV.1612.01474.
[68] E. Sizikova *et al.*, 'Synthetic data in radiological imaging: current state and future outlook', *Oxf. Univ. Press OUP*, vol. 1, Jan. 2024, doi: 10.1093/bjrai/ubae007.
[69] T. Russ *et al.*, 'Synthesis of CT images from digital body phantoms using CycleGAN', *Int. J. Comput. Assist. Radiol. Surg.*, vol. 14, no. 10, pp. 1741–1750, Oct. 2019, doi: 10.1007/s11548-019-02042-9.
[70] B. Khosravi *et al.*, 'Synthetically enhanced: unveiling synthetic data's potential in medical imaging research', *eBioMedicine*, vol. 104, p. 105174, 2024, doi: https://doi.org/10.1016/j.ebiom.2024.105174.
[71] 'TRS 457 - Dosimetry in Diagnostic Radiology: An International Code of Practice', IAEA, Technical Report 457, 2007. Accessed: Apr. 30, 2025. [Online]. Available: https://www-pub.iaea.org/MTCD/Publications/PDF/TRS457_web.pdf
[72] D. Hendrycks and K. Gimpel, 'A Baseline for Detecting Misclassified and Out-of-Distribution Examples in Neural Networks', presented at the ICLR 2017, Toulon, France, 2016. doi: https://doi.org/10.48550/arXiv.1610.02136 Focus to learn more.

Danksagung

Auf der letzten Seite dieser Arbeit möchte ich die Gelegenheit nutzen und den vielen Menschen danken, die mich auf dem Weg der Promotion begleitet und unterstützt haben.

Zunächst möchte ich mich bei Herrn Prof. Dr. Kröninger für die hervorragende Betreuung bedanken. Außerdem spreche ich Herrn Prof. Dr. Armin Lühr meinen Dank für das Lesen und Bewerten meiner Arbeit aus. Weiterhin gilt mein Dank Frau Dr. Ulrike Ankerhold, die als meine Vorgesetzten mir diese Arbeit ermöglicht hat.

Ein besonderer Dank gilt meinem Arbeitsgruppeleiter Herrn Dr. Stefan Pojtinger. Vielen Dank für all deinen Input, deine Begleitung und die vielen fachlichen Diskussionen. Danke fürs Unterstützen und Herausfordern in genau dem richtigen Maße.

Auch Herrn Dr. Jörg Martin gilt mein expliziter Dank für die fachliche Unterstützung.

Als nächstes möchte ich mich bei meiner Arbeitsgruppe 6.25 und meinem Fachbereich 6.2 bedanken. Danke für das positive und unterstützende Umfeld. Danke für alles Mitdenken, Diskutieren, Ermutigen und Lachen. Dieser Dank gilt auch meinen Mitdoktorand*innen und ganz besonders meinen Kolleginnen Carolin Buchmann, Ina Warkehr, Miriam Schwarze und Elisabeth Salomon!

Des Weiteren geht ein dickes Dankeschön zusätzlich an Ludwig, Miriam, Elisabeth, Rebekka und Jessi fürs Korrekturlesen meiner Arbeit.

Meine liebe Familie und Marina: Danke für all eure Liebe, euer Zuhören und eure Unterstützung. Das ist nicht selbstverständlich und ich kann mich so glücklich schätzen euch zu haben.

Zuletzt und nicht in Worte zu fassen, gilt mein Dank meinem Mann Jan-Ard: Du bist mein Halt und mein Zuhause. Danke für deine Ruhe und deine Zuversicht; diese Arbeit hast du in so großem Maße mitgetragen.